Hemodynamic Analysis of Stent Strut Cross-sectional Profiles

Sylvain Pagnier

Biomechanics Lab, McGill University

Supervisor: Rosaire Mongrain

A thesis submitted to McGill University in partial fulfillment of the requirements of the Undergraduate Honours Program

Table of Contents

List of Figures vii
List of Tables vii
Abstract viii
Abrégé ix
Acknowledgements x

1 Introduction **1**
1.1 Overview 1
1.2 Literature Review 3
1.2.1 Disease Pathology and Diagnosis 4
1.2.2 Stent Treatment of Atherosclerosis 5
1.2.3 Stent Design 7
1.2.4 Cardiovascular CFD Research 10
1.2.5 Stent Analysis Metrics 15
1.2.6 Comments on the Necessity of FEA in Cardiovascular Research . . . 16
1.3 Objectives of Current Study 16
1.4 Outline 17

2 Two-Dimensional Model Development **18**
2.1 Overview 18
2.2 Governing Equations 18
2.3 Models Used to Solve the Governing Equations 19

2.3.1 Newtonian and Non-Newtonian Blood Models 19
2.3.2 Turbulence 20
2.3.3 Steady and Transient Flow Models 21
2.3.4 Constant Blood Density and Homogeneity 22
2.3.5 Arterial Wall Rigidity 22
2.3.6 Patient-Specific Geometry 22
2.3.7 Two-Dimensional Model Approximation 22
2.4 Computational Setup 23
2.4.1 Geometry 23
2.4.2 Mesh 25
2.4.3 Boundary Conditions 28
2.4.4 Computational Solver 29
2.5 Model Validation 30
2.5.1 Grid Independence 30
2.5.2 Comparison to Other Research 33
2.5.3 Comparison to an Analytical Solution 36
2.6 Statistical Tools 36

3 Two-Dimensional Model Results **39**
3.1 Overview 39
3.2 Benchmark Results 39
3.3 Streamlined Cross-Sectional Profile Results 40
3.3.1 Fillet Configurations 40
3.3.2 Conic Profiles 41
3.4 Strut Taper Results 42
3.5 Stent Mechanical Parameter Results 43
3.6 The Effect of the Various Blood Models 43
3.7 Discussion of Results 44
3.7.1 Streamlined Cross-Sectional Profile Discussion 45

3.7.2 Strut Taper Discussion 46
3.7.3 Stent Mechanical Parameter Discussion 47
3.7.4 Discussion of the Various Blood Models 51

4 Final Conclusions and Summary **52**
4.1 Limitations and Recommendations 52
4.2 Summary 53

List of Figures

1.1 Cross-sectional view of a presently stable atherosclerotic plaque characterized by a thick fibrous cap [1]. 2
1.2 2-D drawings of a range of modern stents, demonstrating the breadth of possible geometry. Red arrows demonstrate the connectors between stent cells [2]. 4
1.3 Sectional views of the commercial Absorb BVS are shown on the left side with magnified images of the white-boxed areas on the right. Over time, the number of scaffolding discontinuities, indicated by the yellow arrows, increases [3]. 7
1.4 An example of a typical stent geometry with relevant stent design parameters labelled [4]. 8
1.5 Dimensionless pressure streamlines around stent struts of various circular aspect ratios. Of particular interest are the areas of flow recirculation directly adjacent to the stent struts and most visible in the case of non-streamlined struts [5]. 9

2.1 The two-dimensional geometrical half section used to represent a stented human coronary artery, here pictured with rectangular struts. 23

2.2 Geometrical depiction of the various strut fillets used in the CFD simulations. The fillets are of a constant radii and were all parameterized by a fillet strength describing the fillet arc. CFD simulations were performed for cases where there are both fillets present (as pictured), or only one of the two fillets. 25
2.3 Geometrical depiction of the conic struts alongside their defining variable ρ. These conics were used in the various CFD simulations to ascertain the optimal conic stent strut profile. 26
2.4 Geometrical depiction of the strut taper used in the various CFD simulations and its characteristic variable θ. 26
2.5 Two-dimensional stent geometry with relevant stent design parameters indicated by w, h, and l as taken from [6]. Here w was taken to represent strut width, h strut height, and l strut spacing. 27
2.6 An example of the two-dimensional mesh created in ANSYS Fluent used to solve the tapered strut simulations. 27
2.7 Approximate cardiac pulsatile flow profile used to implement the transient boundary condition. This pulsatile waveform was scaled to physiological values more relevant to this thesis and is detailed in Table 2.1. 28
2.8 Points A and B where the WSS was evaluated to indicate spatial, temporal, and cyclic mesh convergence. 31
2.9 Spatial mesh convergence analyzed by progressively refining the spatial mesh from n initial elements. The change in WSS decayed to 0 for a mesh of $8n$ (23,216) elements indicating spatial mesh convergence. 32
2.10 Time-step convergence analyzed by progressively refining the time-step from t initial number of time steps. The change in WSS decayed to a negligible .02 Pa for point B by $100t$, though still indicating the proper decay curve for grid independence, before the simulations became too computationally arduous. 33

2.11 Cyclic convergence analyzed by measuring the change in WSS at points A and B for subsequent cycles after the first cardiac cycle (cycle 0). Results indicated that two subsequent cycles (three total cycles) were necessary for cyclic convergence. 34
2.12 (a) The WSS profile between the first and second stent struts for various strut shapes. The square strut WSS curve (the curve with the lowest average WSS) was used to validate the implemented computational model. (b) Dimensionless WSS (nondimensionalized by the model's physiological WSS) between the first and second stent struts for a square strut used as comparison to the result in (a). One may note the similar dip and recovery of WSS after the first stent strut (start of the x domain) before the flow is again perturbed by the second stent strut (end of the x domain). This qualitative WSS profile agreement was used to help validate the computational model implemented in this thesis. 35
2.13 Analytical and computational comparison of the solution for the velocity profile in a two dimensional plain cylinder. 37

3.1 The effect of the various fillet configurations, and fillet strength, on the traditional risk of restenosis quantified by the percentage of arterial area under .5 Pa in the second intra-strut area. 47
3.2 The effect of changing the conic ρ defining the cross-sectional profile on the traditional risk of restenosis quantified by the percentage of arterial area under .5 Pa in the second intra-strut area. 48
3.3 The effect of the various traditional mechanical parameters on the traditional risk of restenosis. From top to bottom, the mechanical parameter of interest was: strut width, strut height, and strut spacing. 49
3.4 The effect of the various traditional mechanical parameters on the dimensionless streamline deflection parameter. From top to bottom, the mechanical parameter of interest was: strut width, strut height, and strut spacing. . 50

List of Tables

2.1 Summary of boundary conditions. 29

3.1 Statistical WSS and streamline deflection results for the benchmark stent models. 40

3.2 Statistical WSS and streamline deflection results as fillet strength was varied for the bottom fillet configuration. 41

3.3 Statistical WSS and streamline deflection results as fillet strength was varied for the top fillet configuration. 41

3.4 Statistical WSS and streamline deflection results as fillet strength was varied for the combined fillet configuration. 42

3.5 Statistical WSS and streamline deflection results for the various conic strut cross-sectional profiles. 42

3.6 Statistical WSS and streamline deflection results as θ was varied for the tapered stents. 42

3.7 Statistical WSS and streamline deflection results for a changing strut width. 43

3.8 Statistical WSS and streamline deflection results for a changing strut height. 43

3.9 Statistical WSS and streamline deflection results for a changing strut spacing. 44

3.10 Statistical WSS and streamline deflection results for physical modelling variations on the first benchmark model, with the transient model evaluated at the same inlet velocity as the other models (at 3.234 seconds). . . . 44

Abstract

Drug eluting stents are an effective treatment for stenosed coronary arteries, but are hindered by a lingering risk of in-stent restenosis due to areas of low wall shear stress. This thesis analyzed the possible hemodynamic improvements of using streamlined stent cross-sectional profiles in comparison to changing typical parameters such as strut height. This computational fluid dynamic research also evaluated the use of a two-dimensional, non-Newtonian, turbulent, pulsatile coronary blood model with particular application to nanovesicle drug treatments where minimal streamline deflection is desired. It was demonstrated that the optimal streamlined profile is a circular one, and that streamlining significantly improves the wall shear stress performance but negligibly impacts the streamline deflection; instead, it was reductions in stent strut height that most decreased streamline deflection.

Abrégé

Les stents à élution médicamenteuse sont un traitement efficace pour les artères coronaires sténosées, mais sont entravés par un risque persistant de resténose dans le stent en raison des zones de faible contrainte de cisaillement de la paroi. Cette thèse a analysé les améliorations hémodynamiques possibles de l'utilisation de profils transversaux de stent simplifiés par rapport à la modification de paramètres typiques tels que la hauteur de la jambe de force. Cette recherche sur la dynamique des fluides computationnelle a également évalué l'utilisation d'un modèle de sang coronaire bidimensionnel, non newtonien, turbulent et pulsatile avec une application particulière aux traitements médicamenteux à base de nanovésicules où une déviation minimale de la ligne de courant est souhaitée. Il a été démontré que le profil profilé optimal est un profil circulaire, et que le profilé améliore considérablement les performances de contrainte de cisaillement de la paroi mais a un impact négligeable sur la déviation du profilé ; au lieu de cela, ce sont les réductions de la hauteur de l'entretoise de l'endoprothèse qui ont le plus diminué la déviation du profil.

Acknowledgements

I would first like to thank Rosaire Mongrain for his help and guidance during this thesis, and for introducing me to this field of biomechanics that I have come to love. I would also like to thank Evgeny Timofeev for his continued support during my time here at McGill as an advisor and professor. Finally, acknowledgements are not sufficient to thank my family and friends for their support in all things that I do. I cannot express how grateful I am to have them in my life, and each day is made the brighter knowing them.

Chapter 1

Introduction

1.1 Overview

The field of biomechanics may be broadly understood as the study of the mechanics of biological systems. Of particular import to this thesis is a subset of this broad field, where mechanics is specialized to fluid mechanics, and biological systems to the human cardiovascular system. This critical subfield of cardiovascular biomechanics is no less important for its specialization, for its research encompasses the diagnosis, prevention, and treatment of heart diseases most pressing to human health. The root of many of these heart diseases is atherosclerosis, and it is this specific heart disease that concerns the bulk of the research conducted in this thesis.

Atherosclerosis is an immuno-inflammatory disease that causes arterial blockage. This blockage is characterized by the accumulation of fatty deposits which eventually form an atherosclerotic plaque. [1].

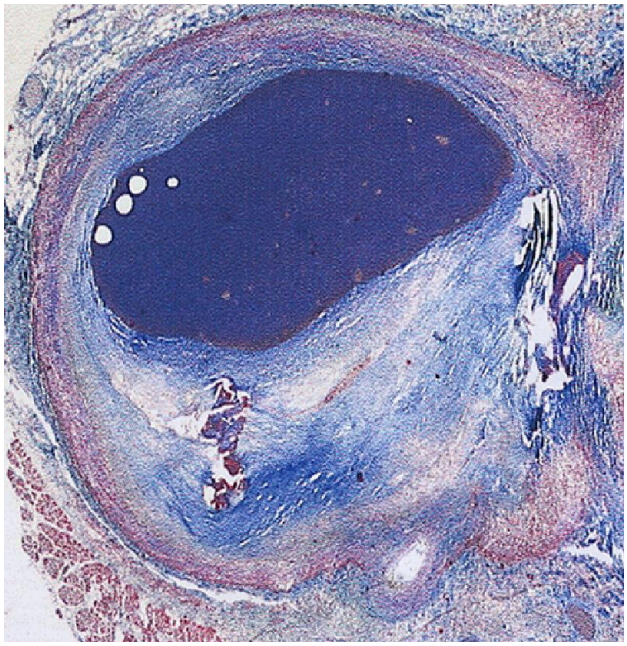

Figure 1.1: Cross-sectional view of a presently stable atherosclerotic plaque characterized by a thick fibrous cap [1].

It is this plaque which is largely responsible for many of the deadly atherosclerotic related diseases, such as heart attacks and strokes [7]. In fact, these diseases are so pervasive that atherosclerosis is responsible for nearly 40% of deaths in developed nations such as the United Kingdom, and cost the United States 151 billion USD in 1996 [8; 9]. Thus, cardiovascular research into atherosclerosis is of the utmost importance.

As cardiovascular research becomes increasingly sophisticated, so too do the means with which atherosclerosis is treated. Historically, atherosclerosis has been treated surgically; coronary artery bypass grafts and percutaneous transluminal coronary angioplasties (PTCA) were the first such methods implemented in the 1960s and 1970s, respectively [7]. However, it is the development of bare metal stents that truly marks the modern age of atherosclerosis treatment. Cardiovascular stents are scaffolding devices typically implanted using a balloon catheter during PTCA [7]. These stents provide support to the diseased artery after surgical intervention to help prevent artery reocclusion, a condition referred to as restenosis. Preventing in-stent restenosis is a primary objective of much cur-

rent cardiovascular research. To this ambition, stent design and research have expanded tremendously to arrive at the modern era of drug eluting stents (DES).

DES operate under the same principles as bare metal stents, but are coated using anti-proliferative drugs that minimize in-stent restenosis. These DES have performed significantly better than the previous era of bare metal stents [10]. However, the importance of research into the mechanical design of the stent must not be understated. The key biological cause of in-stent restenosis is in fact a mechanical one; it is largely areas of low wall shear stress (WSS) and flow stagnation that determine the likelihood of in-stent restenosis [11]. Thousands of stents have been designed over the last 30 years to address this mechanical risk factor, and the various designs result in as much as 13% difference in treatment success rate [12]. Additionally, stent material and geometry affect not only the chance of in-stent restenosis, but also the risk of vascular injury or blood clotting (thrombosis) [13].

Cardiovascular stent research typically exists to complement the stent design cycle. This cycle loops through design ideation, finite element analysis (FEA), computational fluid dynamic (CFD) simulations, and clinical testing. This thesis primarily concerned itself with CFD analysis of the effect of stent cross-sectional streamlining, with particular application to a novel drug eluting technology. This novel drug coating is a stem cell derived nanovesicle that exhibits tremendous potential for treating atherosclerosis with effective anti-inflammatory and pro-arterial elements [14]. This nanovesicle treatment has not only the potential to treat the local surgical site, but also further targeted locations in the human body. This novel targeting mechanic served as motivation for the conducted cardiovascular research.

1.2 Literature Review

This section presents a detailed literature review of modern research in cardiovascular biomechanics. A review of two key implementations of this research will first be pre-

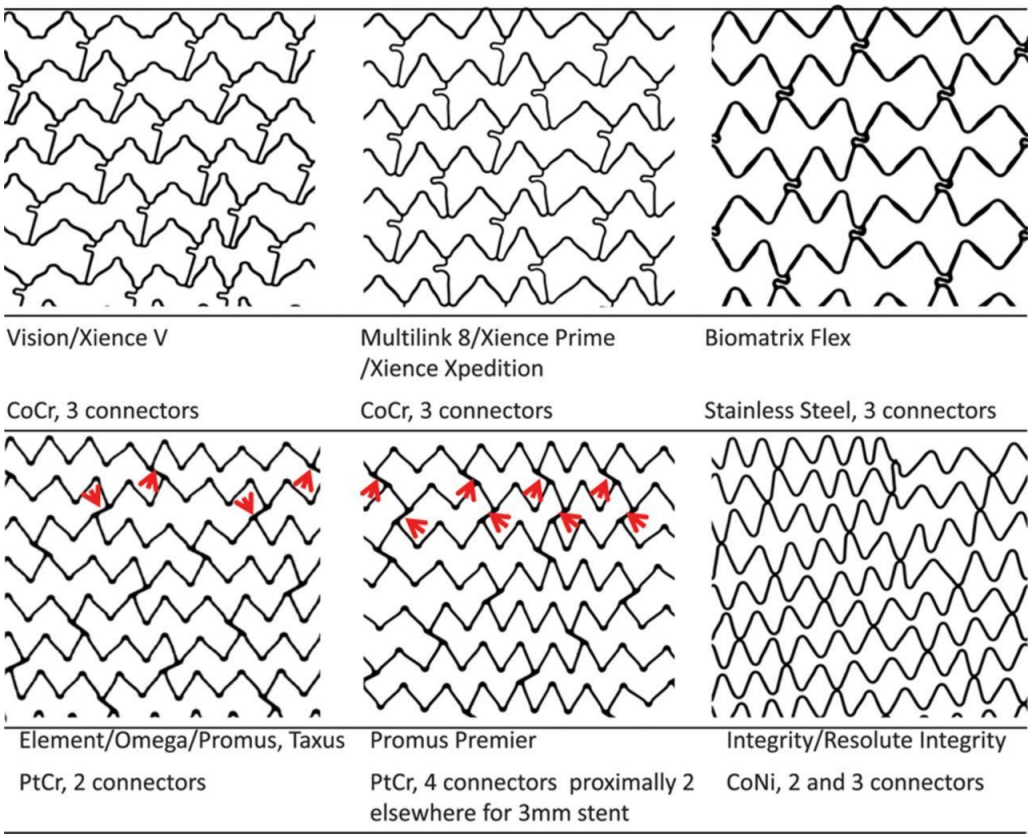

Figure 1.2: 2-D drawings of a range of modern stents, demonstrating the breadth of possible geometry. Red arrows demonstrate the connectors between stent cells [2].

sented, with specific attention being given to the second section delineating stent treatment. Then, research into the design of these stents will be discussed. Next, current cardiovascular CFD methods will be presented alongside the metrics with which the results are quantified. The literature review will conclude with comments on the usefulness of FEA in more holistic research.

1.2.1 Disease Pathology and Diagnosis

Much research into cardiovascular mechanics deals with understanding the pathology of atherosclerosis and can thus be used to diagnose and predict the appearance of the disease. The primary mechanical indicator for atherosclerosis is the presence of zones of low wall shear stress and flow recirculation [11; 15]. Typically, artery vulnerability

is quantified by the arterial area under a critical WSS value of .5 Pa [11]. Biologically, these low shear rates reduce the rate of endothelialization, or the covering of the artery in protective and healthy endothelial cells [5; 16]. This lack of endothelialization is associated with the migration of smooth vascular muscle cells into the vessel wall [17]. Similarly, flow circulation zones serve as reaction chambers for dangerous procoagulant and pro-inflammatory cardiovascular elements [5]. Generally, disturbed flow leads to platelet accumulation and risk of blood clotting and thus a higher risk of contracting heart diseases [18]. As this pathology can be understood in terms of cardiovascular biomechanics, CFD has become a popular tool with which to diagnose patients [19]. Modern diagnostic tools focus on cardiovascular imaging, both to analyze the composition of atherosclerotic plaques and to generate data for CFD diagnostic simulations [20]. This diagnostic CFD research is focusing increasingly on baseline and follow-up studies [18]. By conducting CFD simulations of patient specific geometry in these two studies, it is possible to calculate the changing hemodynamic and vessel parameters over time; this change in parameters helps describe the progression and severity of atherosclerosis [18; 21]. Additionally, understanding these mechanical indicators enables physicians to focus on areas of disturbed flow, such as bifurcations and tortuous geometry, as it is here that atherosclerosis is most commonly found.

1.2.2 Stent Treatment of Atherosclerosis

As mentioned in section 1.1, the development of bare metal stents truly marks the beginning of the modern treatment of atherosclerosis. However, current treatment has improved tremendously since the implementation of the first metal stents. Bare metal stents have evolved into coated DES which better reduce in-stent restenosis, and metal has evolved into more flexible and biocompatible polymers [10]. DES remain the most promising atherosclerotic treatment available today as the risk of restenosis or revascularization is quite low [10]. However, the coating that stores the drug agent is still being improved upon. Polymer coatings typically serve as the drug carrier, but modern studies

indicate that polymer free DES are associated with an 18% reduction in total mortality when compared to traditional polymer coatings [10]. To compensate for this significant difference in mortality, more durable or biodegradable polymer coatings are currently being developed [10]. Additionally, new antiproliferative drug agents are also being developed [10]. One of the more promising new drug agents is a targeting nanovesicle carrier. This mesenchymal stem cell derived nanovesicle has been specially designed to target disturbed flow sites using the peptide PREY through cellular membrane functionalization. [14]. Potent anti-inflammatory and pro-endothelial cell recovery effects have been clinically confirmed using animal and microfluidic disturbed flow testing [14]. Yet, the nanovesicles' circulation half life is only 30 minutes, and thus maintaining proper flow streamlines post-surgery is imperative for full utilization of this nanovesicle treatment.

Interestingly, stent installation is typically only necessary for one year post-surgery until the artery has recovered its natural form; however, the aforementioned stents are all permanent installations. This permanency exposes a deadly risk of long-term stent fracture and tissue inflammation [22]. A promising new development in the form of bioresorbable vascular scaffolds (BVS) seeks to address this flaw. BVS have been developed mainly using bioresorbable polymers such as PLLA and can thus be broken down safely when no longer needed. PLLA has added benefits of a reduced stent recoil (reduction in stent diameter after balloon expansion) and a reduction in balloon expansion complications [22].

Disappointingly, current BVS have proved ineffective in clinical trials, and in fact increase the incidence of blood clotting, though newer studies indicate that BVS are improving [10]. A potential explanation for this performance is the less-efficient scaffolding geometry necessitated by inferior BVS material properties [10]. Nonetheless, it is clear that BVS present a promising evolution of the modern DES.

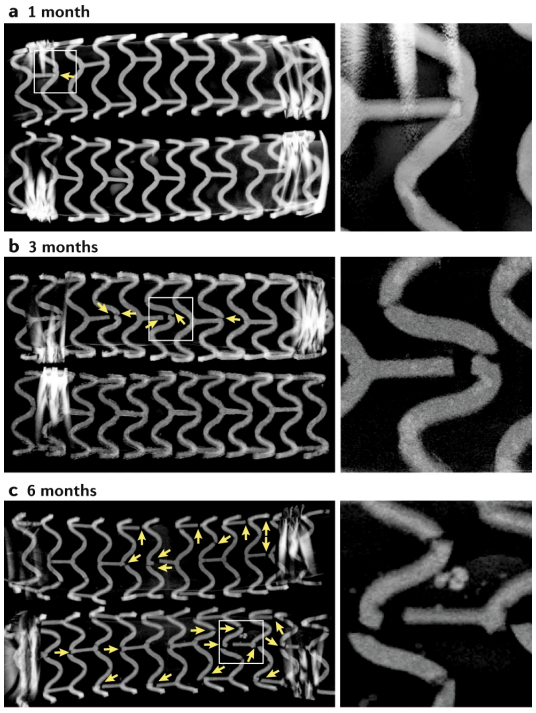

Figure 1.3: Sectional views of the commercial Absorb BVS are shown on the left side with magnified images of the white-boxed areas on the right. Over time, the number of scaffolding discontinuities, indicated by the yellow arrows, increases [3].

1.2.3 Stent Design

Just as the nature of stents has become increasingly sophisticated, so too has stent geometrical design. Copious research has been performed on the effect of various stent geometries on overall hemodynamic performance in an effort to ascertain the most crucial design parameters.

Of particular note is strut height and strut spacing, referred to as strut thickness and ring spacing, respectively, in Figure 1.4. Strut height is typically regarded as the most crucial mechanical parameter for minimizing in-stent restenosis and thrombogenicity [23; 24]. Correspondingly, stent designs have sought to minimize strut height. Typically, modern polymeric DES have strut heights around $80\,\mu\mathrm{m}$, though this value is typically a bit lower at $70\,\mu\mathrm{m}$ for metal stents [25]. Yet, these strut heights are limited by stent fatigue and scaffolding requirements. To achieve thinner struts while satisfying these

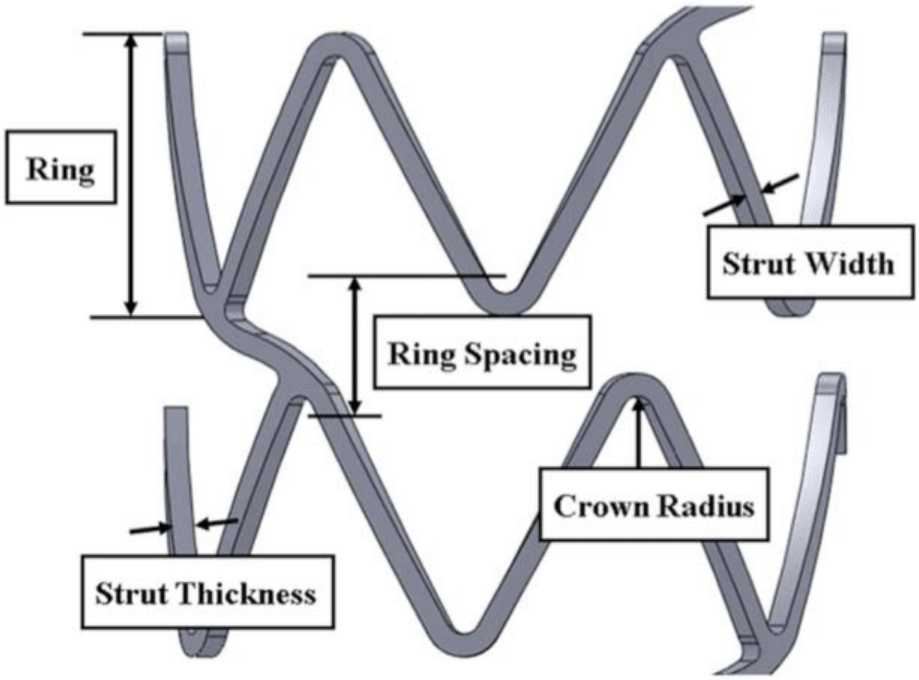

Figure 1.4: An example of a typical stent geometry with relevant stent design parameters labelled [4].

constraints, some designs have implemented a tapered stent profile. This tapered stent profile is defined by a reduction in strut height along the strut spacing. This tapering enhances fatigue strength and enables strut height to decrease to half of its non-tapered value in the midpoint of the ring spacing [26]. Strut spacing, too, is a crucial stent design parameter. Areas of small strut spacing are correlated with critically low values of WSS [27]. In fact, strut spacing is widely regarded as the most important parameter for determining flow stagnation patterns [28]. Achieving a balance between hemodynamic and mechanical performance is at the crux of modern stent design. While not indicated in Figure 1.4, strut embeddedness – the percentage of the strut height absorbed into the inner arterial wall – is also quite important, especially for DES design. Numerous clinical and CFD studies have been performed to ascertain the ideal strut embeddedness, and typically agree that DES perform best when half-embedded [23]. However, as the optimization of these stent mechanical parameters becomes limited by practical design constraints, it becomes necessary to analyze the effect of other stent geometrical features.

One such less researched parameter is the effect of streamlining the stent strut cross-sectional profile. Non-streamlined struts promote flow conditions with recirculation and low WSS [5; 17; 23]. Furthermore, more streamlined stent profiles inhibit neointimal growth, a precursor to in-stent restenosis [29]. In fact, while these effects have been less researched, clinical studies indicate that streamlining stent profiles possibly has a bigger impact than strut height for minimizing in-stent restenosis and thrombosis [29].

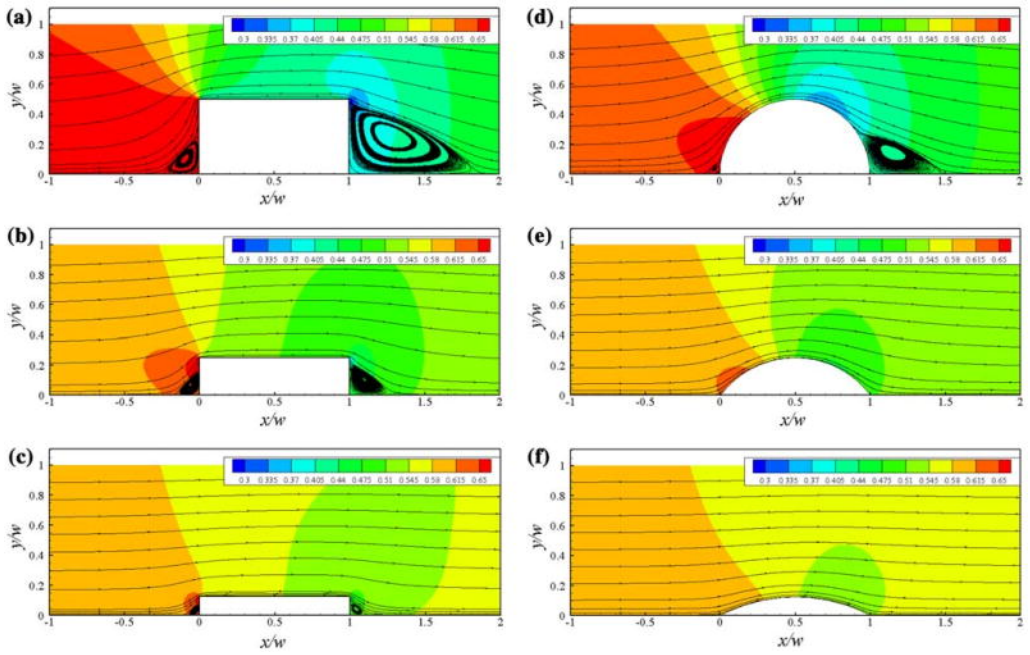

Figure 1.5: Dimensionless pressure streamlines around stent struts of various circular aspect ratios. Of particular interest are the areas of flow recirculation directly adjacent to the stent struts and most visible in the case of non-streamlined struts [5].

Current research indicates that streamlined struts will always perform better than non-streamlined ones of the same geometry [17]. Furthermore, among the possible streamlined designs, it is the ellipse that is most ideal, even when compared to the teardrop profile [23]. This result is also practically significant as elliptical cross sections are easily obtained by chemically etching rectangular profiles [23].

1.2.4 Cardiovascular CFD Research

As this thesis dealt primarily with cardiovascular CFD simulations, it is necessary to outline the current best practice in the field. This section will begin with an outline of the relevant governing equations, and most importantly, the simplified models used to solve them. Details will then be provided for common boundary conditions and relevant physiological flow parameters. Finally, choice of mesh and physics solvers will be discussed.

Governing Equations

The principle governing equations for cardiovascular biomechanics, specifically for coronary blood flow, are the conservation of mass, momentum, and energy. Additionally, these equations are often implicitly constructed assuming that the bulk viscosity of the fluid is zero. The corresponding conservation laws are here expressed as the typical set of Navier-Stokes equations (provided in full in [30]), though neglecting body forces and external heat:

$$\frac{\partial \rho}{\partial t} + \nabla \cdot (\rho \mathbf{V}) = 0 \tag{1.1}$$

$$\frac{\partial (\rho \mathbf{V})}{\partial t} + \nabla \cdot \rho \mathbf{V}\mathbf{V} - \nabla \cdot \mathbf{\Pi}_{ij} = 0 \tag{1.2}$$

$$\frac{\partial (E_t)}{\partial t} + \nabla \cdot \ E_t \mathbf{V} + \nabla \cdot \mathbf{q} - \nabla \cdot (\mathbf{\Pi}_{ij} \cdot \mathbf{V}) = 0 \tag{1.3}$$

where ∇ represents the vector differential operator, $\mathbf{\Pi}_{ij}$ the stress tensor, $\mathbf{V}$ the velocity vector, ρ the fluid density, E_t the total energy per unit volume, and $\mathbf{q}$ the heat flux. The heat flux and stress tensor may be further expanded to better represent the physical phe-

nomena represented in equations 1.1-1.3:

$$\mathbf{q} = -k\nabla T \tag{1.4}$$

$$\mathbf{\Pi}_{ij} = -p\delta_{ij} + \tau_{ij} \tag{1.5}$$

$$\tau_{ij} = \mu[(\frac{\partial(u_i)}{\partial x_j} + \frac{\partial(u_j)}{\partial x_i}) - \frac{2}{3}\delta_{ij}\frac{\partial(u_k)}{\partial x_k}] \tag{1.6}$$

where T represents the temperature, k the coefficient of thermal conductivity, u_i components of velocity, p the pressure, δ_{ij} the Kronecker delta function, and μ the coefficient of viscosity.

These equations are highly non-linear and hence difficult to solve in their general form. Thus, it is necessary to simplify the physics models.

Newtonian and Non-Newtonian Blood Models

Blood is properly a non-Newtonian, viscoelastic, thixotropic shear-thinning fluid; however, modelling this behavior remains computationally intense. Perhaps the most crucial cardiovascular assumption is on how best to simplify this complex behavior. Assuming Newtonian behavior is often thought to be valid at high strain rates, and is quite common in research [31]. However, more recent CFD studies indicate significant differences in hemodynamic parameters, such as WSS, between non-Newtonian and Newtonian blood models [32]. When blood is taken to be Newtonian, its viscosity is typically taken to be 3.5 mPa-s [23; 27; 28; 33]. On the other hand, there is less agreement among authors as to which non-Newtonian model is best. The most common non-Newtonian models include the power law, Casson, Carreau, and generalized power law models [34]. While these models differ in construction, their WSS distributions demonstrate significant agreement, particularly when compared to the results of the Newtonian model [31]. Hence, while most research takes blood to be Newtonian, it is likely that the simplification is not valid [32]. In particular, assuming a Newtonian model for blood leads to severe model in-

accuracies in concave regions, such as near coronary artery bifurcations, as these areas demonstrate patches of highly non-Newtonian behavior [31].

Turbulence

Cardiovascular blood flow is often taken to be laminar, though several turbulence models have been proposed to interesting effect. Laminar flow is commonly thought to be valid for healthy arteries but severely stenosed arteries are more likely to exhibit transitional or turbulent flow [32]. When modelling blood flow turbulence it is common to use the k-epsilon or k-omega models [15]. Both models predict higher WSS than in laminar flow, with the k-epsilon model predicting the highest WSS level. Hence, laminar flow may be viewed as a conservative assumption as it overestimates the risk of restenosis [15]. However, to best model blood turbulence one must account for the red blood cells within the blood. Preliminary studies indicate that these red blood cells affect turbulence and general flow parameters as, in smaller length scales, it is these cells that absorb flow momentum [35]. Furthermore, the viscous cell to cell interactions within the flow may affect the pertinent hemodynamic flow parameters [35]. Nonetheless, assuming a laminar regime in all geometries is still common, and research indicates it is an assumption with fewer consequences than assuming a Newtonian flow, for example [15].

Steady and Transient Flow Models

Blood flow, especially in comparative studies, is often analyzed in the steady state. This assumption is often viewed to be relatively harmless, while greatly simplifying computational cost [23; 33]. Yet, coronary blood flow is truly a transient, pulsatile phenomenon, and some studies have treated it as such and found noticeable differences between the two models [15; 28].

Constant Blood Density and Homogeneity

Possibly the most common assumption in cardiovascular biomechanics is taking blood to have a constant density. Certainly, it is thought that blood has a similar compressibility to distilled water, and is independent of its number of red blood cells [36; 37]. The vast majority of numerical studies have analyzed blood flow in this macroscopic, homogeneous way to great effect [32]. And yet, recent literature indicates that it may be necessary to model blood components, such as plasma, separately [32]. This model of blood homogeneity is particularly ineffective near flow stagnation zones due to the accumulation of cells [38]. In fact, some research indicates that the continuum assumption behind most fluid dynamic theory may not be valid in some blood flow analyses; though, it is more critical for small vessel diameters within an order of magnitude of red blood cell length scales [35].

Arterial Wall Rigidity

It is also common to assume rigid arterial walls in cardiovascular CFD simulations, though newer research indicates that this may not be valid. Older research typically indicates that the rigid wall assumption is valid with little consequence, and this is still generally thought to be true for comparative CFD studies [23; 28; 34]. However, more recent simulations indicate that ignoring vessel compliance may have a greater effect even than assuming blood to be Newtonian [15]. Arterial wall compliance is often modelled using non-linear isotropic hyperelastic models that depend also on the severity of the vessel stenosis [32]. Furthermore, the fluid-structure interaction may also be significant, and thus newer numerical studies have begun to account for this interaction [21].

Patient-Specific Geometries

Advancements in imaging technology have also enabled coronary blood flow analysis in patient specific geometries. These 3D geometrical images are often captured using

magnetic resonance and computed tomography due to their accuracy [32]. When available, these geometries facilitate the diagnosis of atherosclerosis as well as a more accurate capturing of hemodynamic parameters [15; 16; 31; 32]. Nonetheless, it is still typical to assume a straight vessel geometry, especially for more general studies [23]. For example, the coronary artery is often taken to be a 3-4 mm diameter straight tube [23; 28].

Physiological Flow Parameters and Boundary Conditions

Cardiovascular blood flow is further complicated by the variance in physiological flow parameters and thus flow boundary conditions. These flow parameters are not universal and depend on a myriad of factors such as age and health. Typically, coronary blood simulations take the inlet flow to be fully developed, with an average flow speed of around .2-.3 $\frac{\text{m}}{\text{s}}$ [23; 27]. Most analyses agree that the inlet flow ought to be purely axial, in both steady and transient analysis. However, some newer research indicates that more accurate simulations may be performed if the inlet is taken to instead be a pressure boundary equal to the systemic coronary pressure [33]. These boundary conditions may be made further accurate if the boundary conditions are made patient specific with input from upstream and downstream circulatory system components; though, this may not be ideal in the case of non-diagnostic analysis [33; 34]. Generally, the flow outlet is taken to be a zero pressure outlet [23; 28; 33]. Physiologically, the blood flow inlet velocity ought to be pulsatile, with around a .8 s period and a peak Reynolds number ranging from 150 to 460 [28; 33]. To ensure a fully developed inlet waveform in transient analysis, studies often enlarge inlet and outlet lengths to more than 5 times the vessel diameter [23; 27].

Computational Solver and Mesh

The aforementioned governing equations are typically solved with the finite volume method. While there is no common preference among the various computational solvers, it is common to use ANSYS Fluent for cardiovascular research [27; 32].

Within ANSYS Fluent, it is typical to use double precision segregated solvers with second-order windward schemes to discretize the differential equations [27; 34]. Typically, the preferred ANSYS Fluent algorithm for solving the pressure discretization is SIMPLE or SIMPLE-C, due to their robust nature and rapid convergence. A satisfactory mesh is typically generated using linear quadrilateral elements, though tetrahedral elements are preferred for stented segments in three dimensions [23; 27].

1.2.5 Stent Analysis Metrics

To effectively characterize the performance of any stent design it is important to establish relevant qualitative metrics. Traditionally,in-stent restenosis is taken to be correlated to the percentage of arterial area under a critical WSS value of .5 Pa [23]. Some research has improved on this static critical value and instead implemented various more detailed statistical tools. Stent performance may instead be characterized using the mean, standard deviation, and kurtosis of its WSS profile [23]. Furthermore, to promote standard analysis across a host of studies, it was proposed to nondimensionalize these statistical tools. The mean is divided by the average WSS of a healthy artery (around 2.5 Pa), the standard deviation by the mean, and the kurtosis by the dimensionless mean [23]. These values are respectively called the dimensionless mean, the coefficient of variation, and the kurtosis coefficient. It ought to be noted that a higher kurtosis coefficient here implies flatter, and thus higher, average WSS values [23]. Stents with reduced risk of restenosis are represented by a higher dimensionless mean, lower coefficient of variation, and higher kurtosis coefficient. These values are typically analyzed between the first two stent struts and assumed to represent all other intra-strut areas, though in this thesis they were measured in the second intra-strut area due to transient effects [23]. Current research concurs that while there is a slight WSS decrease every strut, it is not significant [27].

1.2.6 Comments on the Necessity of FEA in Cardiovascular Research

While not the direct subject of this thesis, it is imperative to review the importance of FEA in cardiovascular research. As mentioned in the overview, stents are often deployed using balloon angioplasty. This procedure includes crimping the stent onto the deployment balloon that is expanded in the artery. This deployment procedure subjects the stent to high stresses and deformations. To design a stent for these mechanical stresses, it is necessary to perform FEA analysis. Stent geometry is crucial for determining stent radial strength, foreshortening rate, stent final diameter, and stent coverage [39; 40]. The ideal stent must have a low profile to be securely crimped, but sufficiently flexible to be deliverable via angioplasty [2]. Furthermore, stents must also be strong enough to resist elastic recoil during continual deformation of the arterial wall [2].

Stent design is a balancing act, here between strength and flexibility. Stents must sufficiently scaffold the vessel to prevent tissue prolapse, but conform to the vessel curvature to prevent distortion [2; 41]. Stents must be strong enough to resist the mechanical stresses, but be constructed of a radio-opaque material to facilitate clinical usage [2]. The stent geometrical parameters relevant to FEA are also those relevant to CFD analysis. To this end, numerous authors argue that stent design must necessarily be a multidisciplinary design optimization problem. Thus, one cannot view the cardiovascular design of stents only with CFD, but with a combination of all relevant design tools.

1.3 Objectives of Current Study

Motivation for this thesis was much the same as that behind all biomechanics, the improvement of human health. Specifically, this thesis sought to reduce lethal complications such as thrombosis and restenosis related to atherosclerotic treatment. To this aim, this research was tailored to complement the most promising drug-eluting technology available, such as the aforementioned nanovesicle drug treatment, which necessitated new metrics of analyzing streamline deflection [14].

Accordingly, the primary objective of this thesis was to find the optimal stent strut cross-sectional profile to minimize streamline deflection and stented area at risk of restenosis. Additionally, this hemodynamic analysis was to be performed with state-of-the art methods and fluid models. The various streamlined profiles were conics and fillets to match realistic manufacturing capabilities and physiological conditions. Specifically, the conic and top fillet profiles match chemical polishing capabilities, while the bottom fillet represents the geometry formed during the re-endothelialization of an embedded strut. To complement this primary objective, there were also a number of sub-objectives. These sub-objectives included the investigation of general stent mechanical parameters – such as changing strut height and strut taper – and quantifying the effect of using more complicated blood models. Additionally, this thesis implemented new statistical methods to analyze WSS and streamline deflection.

1.4 Outline

The remaining sections of this thesis deal with the specifics of the developed two-dimensional CFD model as well as the analysis and summary of its results. Chapter 2 will summarize the relevant physical models and computational tools required to solve the governing equations, as well as reiterating the implemented statistical tools. Chapter 3 concerns the results of the CFD model for the various streamlined profiles and mechanical stent design parameters. Finally, chapter 4 will summarize the conclusions of this thesis, as well as mentioning limitations and recommendations for future research.

Chapter 2

Two-Dimensional Model Development

2.1 Overview

This section will outline the means of developing and implementing a two-dimensional computational model used to characterize stent hemodynamic performance. The relevant governing equations will be reiterated alongside the chosen simplifying physical models used in solving those governing equations. The necessary computational setup is then described, detailing the relevant analyzed geometrical parameters and corresponding mesh, boundary conditions, and chosen computational solver. Model verification, in the form of mesh convergence analyses and comparisons to past research and analytical solutions, is then demonstrated. Finally, the utilized hemodynamic statistical tools will be restated.

2.2 Governing Equations

The relevant governing equations are the same Navier-Stokes equations described in section 1.2.4 (equations 1.1-1.6). However, it is also necessary to introduce the relevant dimensionless numbers used to facilitate solving these governing equations.

Of particular interest are the Reynolds (Re) and Womersley (Wo) numbers. These two dimensionless numbers both represent the relative strength of inertial forces to viscous

forces in the flow, with Wo being the pulsatile flow analog of the Re number. In fact, Wo may be related to Re through another dimensionless number describing the inertial forces due to convective acceleration. However, here the Re and Wo numbers are expressed independently for the sake of brevity:

$$\text{Re} = \frac{\rho u L}{\mu} \tag{2.1}$$

$$\text{Wo} = L(\frac{\omega \rho}{\mu})^{\frac{1}{2}} \tag{2.2}$$

where ρ represents the fluid density, u the flow speed, ω the angular frequency of the flow's oscillations, μ the dynamic viscosity, and L an appropriate length scale. For blood flow, it is typical to use the vessel diameter as the characteristic length in both dimensionless parameters. These dimensionless numbers are used in section 2.4.3 to describe the nature of the inlet velocity waveform.

2.3 Models Used to Solve the Governing Equations

This section concerns the choice of relevant physical models used to solve the governing equations. It is necessary to seek a balance between physical accuracy and computational cost, and the chosen compromises are detailed here. Context for these choices is presented in length in section 1.2.4.

2.3.1 Newtonian and Non-Newtonian Blood Models

Current research indicates that modelling blood as Newtonian results in significant errors compared to its true behavior in areas of low shear [34]. Correspondingly, non-Newtonian models – though still a simplification – provide more accurate results [21]. This thesis specifically used the generalized power-law model to model blood due to its superior ability in approximating blood molecular viscosity and WSS [18; 31; 34]. In the

generalized power-law model taken from [34], blood viscosity is represented as:

$$\mu = \lambda|\dot{\gamma}|^{n-1} \tag{2.3}$$

where

$$\lambda(\dot{\gamma}) = \mu_\infty + \Delta\mu \exp\left[-(1 + \frac{|\dot{\gamma}|}{a}) \exp\left(\frac{-b}{|\dot{\gamma}|}\right)\right] \tag{2.4}$$

$$n(\dot{\gamma}) = n_\infty - \Delta n \exp\left[-(1 + \frac{|\dot{\gamma}|}{c}) \exp\left(\frac{-d}{|\dot{\gamma}|}\right)\right] \tag{2.5}$$

Here $\mu_\infty = .00345$, $n_\infty = 1.0$, $\Delta\mu = .25$, $\Delta n = .45$, $a = 50$, $b = 3$, $c = 50$, and $d = 4$. This generalized power-law model was implemented in ANSYS Fluent using an appropriate user defined function.

2.3.2 Turbulence

While blood flow is commonly assumed to be laminar, the assumption may lead to physical inaccuracies. Notably, the plasma rich blood at the edges of the flow exhibits high frequency fluctuations that indicate turbulence [35; 42]. Thus, it may be necessary to choose an appropriate turbulent flow model to best capture the hemodynamic parameters near the arterial wall. The shear stress transport (SST) $k-\omega$ turbulence model was chosen as it exhibits the best results near the arterial wall [19]. This SST $k-\omega$ model is a blending of the standard two-equation eddy viscosity models $k-\omega$ and $k-\epsilon$ to best capture the effects of the boundary layer [19]. The implementation of this SST $k-\omega$ model is taken from [15], where the $k-\epsilon$ transport equations are represented as:

$$\frac{\partial k}{\partial t} + \frac{\partial(\rho k u_i)}{\partial x_i} = \frac{\partial}{\partial x_j}[(\mu + \frac{\mu_t}{\sigma_k})\frac{\partial k}{\partial x_j}] + G_k + G_b - \rho\epsilon - Y_M + S_k \tag{2.6}$$

$$\frac{\partial(\rho\epsilon)}{\partial t} + \frac{\partial(\rho\epsilon u_i)}{\partial x_i} = \frac{\partial}{\partial x_j}[(\mu + \frac{\mu_t}{\sigma_\epsilon})\frac{\partial \epsilon}{\partial x_j}] + C_{1\epsilon}\frac{\epsilon}{k}(G_k + G_{3\epsilon}G_b) - C_{2\epsilon}\rho\frac{\epsilon^2}{k} + S_\epsilon \tag{2.7}$$

and the $k-\omega$ transport equations are written as:

$$\frac{\partial(\rho k)}{\partial t} + \frac{\partial(\rho k u_i)}{\partial x_i} = \frac{\partial}{\partial x_j}[\Gamma_k\frac{\partial k}{\partial x_j}] + G_k - Y_k + S_k \tag{2.8}$$

$$\frac{\partial(\rho\omega)}{\partial t} + \frac{\partial(\rho\omega u_i)}{\partial x_i} = \frac{\partial}{\partial x_j}[\Gamma_\omega\frac{\partial \omega}{\partial x_j}] + G_\omega - Y_\omega + S_\omega \tag{2.9}$$

In these transport equations, G_k represents the turbulent kinetic energy generation due to velocity gradients, G_b the turbulent kinetic energy generation due to buoyancy, G_ω the generation of ω, Y_M the contribution of fluctuating dilatation to the dissipation rate, and μ_t the turbulent viscosity. Additionally, S_k, S_ϵ, and S_ω are source terms while $C_{1\epsilon}$, $C_{2\epsilon}$, and $C_{3\epsilon}$ are constants and σ_k, σ_ϵ respectively represent the turbulent k and ϵ Prandtl numbers. Finally, Γ_k and Γ_ω respectively represent the effective diffusivity of k and ω, while Y_k and Y_ω represents their turbulent dissipation [15]. For sake of brevity, further deconstructions of these equations and the values of the parameters are not described here but are included in full at [15].

2.3.3 Steady and Transient Flow Models

Cardiovascular blood flow is inherently of a transient, pulsatile nature, but is often approximated as steady flow due to computational cost. However, steady flow analyses typically misrepresent the true physics by overestimating areas of low WSS [27]. Ergo, it was deemed necessary to model this transient behavior by implementing a pulsatile inlet waveform to match the cardiac cycle. Furthermore, to compensate for the added computational cost, this transient waveform was made to be fully developed.

2.3.4 Constant Blood Density and Homogeneity

While modern literature is beginning to challenge the assumption of taking blood to be homogeneous, no satisfactory heterogeneous models have yet been proposed. Hence, it was necessary to continue with this assumption and ascribe blood a constant density of $\rho = 1060\frac{\text{kg}}{\text{m}^3}$. This physiological blood density value is well in line with modern cardiovascular studies, and the consequences of the assumption are generally thought to be minimal [16; 23; 27; 28].

2.3.5 Arterial Wall Rigidity

While modelling arterial wall compliance is critical for a more holistic understanding of the physics, studies indicate it may not be necessary for comparative CFD studies [23; 27]. Furthermore, some literature indicates that, for CFD research, vessel wall compliance may even have a negligible effect [28]. Thus, largely for the sake of minimizing computational cost, this research modelled the arterial wall as rigid.

2.3.6 Patient-Specific Geometry

Unfortunately, due to a lack of clinical imaging data, it was not possible to incorporate realistic arterial wall geometry into the studies. Furthermore, some studies do indicate that true arterial geometry is not necessary in comparative CFD studies such as was performed in this thesis [23].

2.3.7 Two-Dimensional Model Approximation

To offset the computational cost of the previous blood models, it was deemed prudent to perform the CFD analysis in two-dimensions only. This assumption stems from the axial symmetry present in stented arterial geometries, and is justified by its use in other comparative CFD studies such as [11; 23; 43].

2.4 Computational Setup

This section details the computational setup in ANSYS Fluent used to solve the governing cardiovascular equations. The chosen two-dimensional geometry and geometrical parameters used in the simulations are first detailed. The necessary mesh, boundary conditions, and computational solver used to perform the simulations are also then described.

2.4.1 Geometry

A two-dimensional half section of a human coronary artery was chosen as the base geometry and can be seen in Figure 2.1, while the relevant geometrical parameters are detailed in subsequent subsections. Only the top half of the geometrical section was required as the hemodynamics were assumed to be symmetrical over the center axis. The artery has a diameter of 3.5 mm and a length of 18 mm so as to represent a general coronary artery [23]. No distinction is made between the various tissues composing the arterial wall due to the simplifying rigid wall assumption.

Figure 2.1: The two-dimensional geometrical half section used to represent a stented human coronary artery, here pictured with rectangular struts.

It was chosen to have 5 stent struts as that number has proved sufficient to capture the relevant hemodynamics of a stented arterial segment [7]. This base rectangular stent design was then geometrically altered to analyze the effect of streamlined struts, strut tapering, and general mechanical stent parameters on the stent hemodynamic performance.

Filleted Struts

The first streamlined stent strut profiles were constructed using constant radii fillets parameterized by a fillet radius. This fillet radius was then nondimensionalized and referred to as fillet strength, where fillet strength = $\frac{\text{fillet radius}}{.5(\text{strut height})}$. Fillet strength ranged from zero to one, where one represented the instance in which the fillet radius was equal to half the strut height, equivalent to a circular strut. These fillets were constructed at the arterial wall interface (bottom fillet) and at the furthest flow interface (top fillet); these fillets are pictured in Figure 2.2 to better clarify the geometry. It should again be noted that the bottom fillet represented the profile formed during re-endothelialization (when the healthy arterial cells migrate back onto the embedded strut) and the top fillet represented the profile formed by chemical polishing. Various simulations were performed by changing the fillet strength when one of or both of the fillets were present.

Conic Struts

Conics were the second streamlined stent strut profile to be analyzed. The conic strut shape was used to directly replace the traditional rectangular strut while maintaining its strut height. These conics were defined using the parameter ρ which was varied from .05 to .925 to represent a range of struts from a flattened ellipse to a triangular hyperbola. An example of a conic used in the two-dimensional CFD simulations is pictured in Figure 2.3, where ρ is such to create an elliptical stent strut.

Tapered Struts

Tapered struts were implemented by tapering the strut connectors from a variable point along the strut height. Thus, tapered struts affect the hemodynamics not of the intra-strut area, but of the connectors forming the walls of the intra-strut area. This taper was defined by an angle θ formed between the strut taper and the horizontal axis (the flow direction). This strut taper and defining angle θ are pictured in Figure 2.4. In the

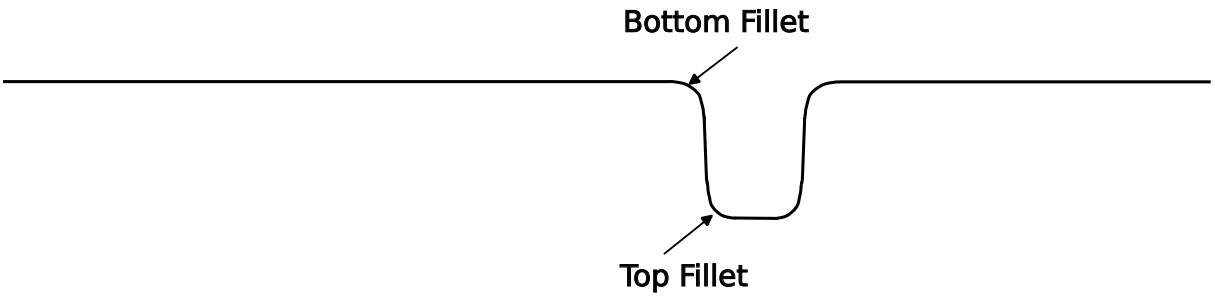

Figure 2.2: Geometrical depiction of the various strut fillets used in the CFD simulations. The fillets are of a constant radii and were all parameterized by a fillet strength describing the fillet arc. CFD simulations were performed for cases where there are both fillets present (as pictured), or only one of the two fillets.

various CFD simulations, theta was varied from 0 to 4.5 degrees whereupon the stent strut height was fully tapered.

Stent Mechanical Parameters

The various stent mechanical parameters analyzed in this thesis were strut width, strut height, and strut spacing. These three parameters are indicated in Figure 2.5 to clarify the nomenclature.

2.4.2 Mesh

The mesh was constructed using linear quadrilateral elements as previous research indicates these elements are well suited to two-dimensional cardiovascular CFD simula-

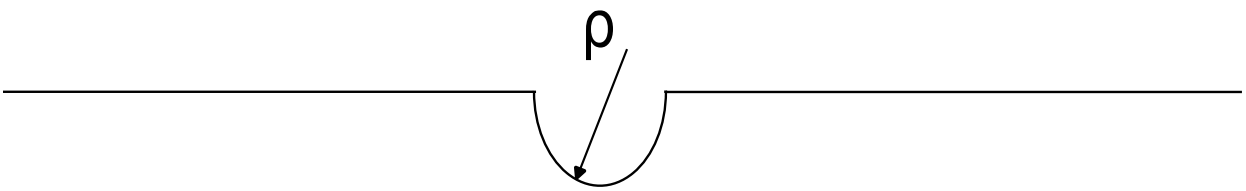

Figure 2.3: Geometrical depiction of the conic struts alongside their defining variable ρ. These conics were used in the various CFD simulations to ascertain the optimal conic stent strut profile.

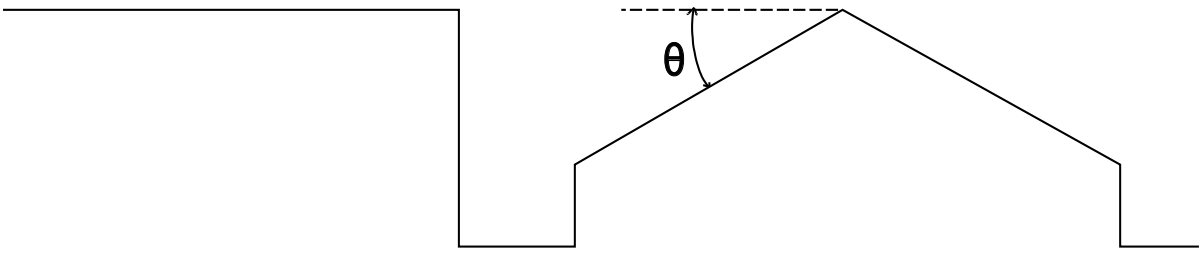

Figure 2.4: Geometrical depiction of the strut taper used in the various CFD simulations and its characteristic variable θ.

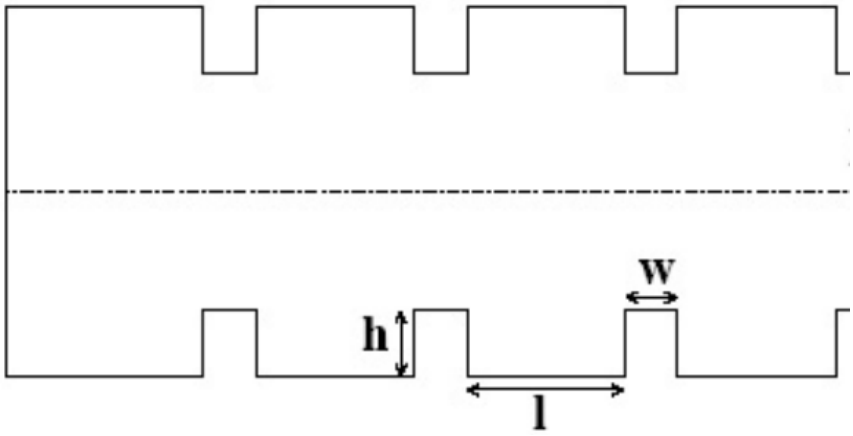

Figure 2.5: Two-dimensional stent geometry with relevant stent design parameters indicated by w, h, and l as taken from [6]. Here w was taken to represent strut width, h strut height, and l strut spacing.

tions [23]. An inflation layer was also created on the stent wall to best capture the turbulent and non-Newtonian flow behavior. Additionally, as this research dealt with fillet radii down to 8 micrometers it was deemed necessary to manually force the mesh into capturing the curvature. Furthermore, mesh convergence analyses (details provided in section 2.5.1) were performed to calculate the required number of elements at 23,216 for accurate simulations. An example of the mesh for a tapered strut length may be seen in Figure 2.6.

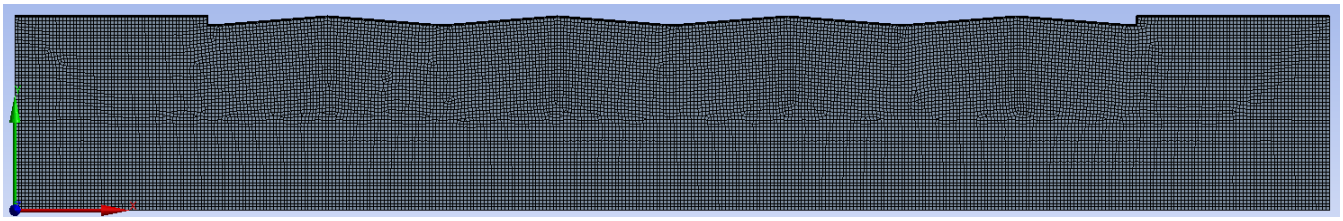

Figure 2.6: An example of the two-dimensional mesh created in ANSYS Fluent used to solve the tapered strut simulations.

The flow was primarily in the x-axis (horizontal direction) with the y-axis (vertical direction) flow being caused by flow perturbations due to the stented geometry. As this model was two-dimensional, the z-direction (out of the page) was neglected.

2.4.3 Boundary Conditions

Before delineating the relevant boundary conditions it is important to characterize the physics using the dimensionless parameters described in section 2.2. These dimensionless numbers were calculated by approximating blood to be a Newtonian fluid with μ = 3.5 mPa-s and a heart beat of 120 beats per minute with an average inlet velocity of .18 $\frac{m}{s}$. Using these physiological values, it was found that Re = 187 and Wo = 4.83 using equations 2.1 and 2.2, respectively. These values agreed with the physiological and dimensionless values outlined in section 1.2.4. Wo was neither small nor large, as is expected in a coronary artery, and thus the pulsatile inlet velocity waveform was approximated as a fully developed Poiseuille flow [44].

To account for the transient, pulsatile nature of the flow, it was decided to implement an approximate pulsatile flow profile as the inlet condition. The pulsatile nature of the inlet was taken from [45] and can be seen in Figure 2.7, but was scaled to more accurate entrance values detailed in Table 2.1.

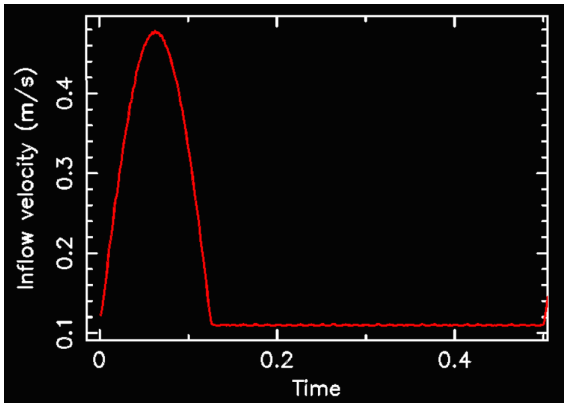

Figure 2.7: Approximate cardiac pulsatile flow profile used to implement the transient boundary condition. This pulsatile waveform was scaled to physiological values more relevant to this thesis and is detailed in Table 2.1.

The implemented inlet waveform was scaled to a physiological peak center velocity of .265 $\frac{m}{s}$ and a resting center velocity of .125 $\frac{m}{s}$. Additionally, due to the Wo calculations,

Table 2.1: Summary of boundary conditions.

Location	Flow Condition
Domain	$\mathbf{V_z} = 0$
Inlet	$\mathbf{V_y} = 0$
	$\mathbf{V_x} = \begin{cases} .265u(\sin(2\pi(t+0.016))), & \text{if } .265(\sin(2\pi(t+0.016))) > .125 \\ .125u, & \text{otherwise} \end{cases}$
	where $u = (1 - (\frac{y^2}{.00175^2}))$
Exit	Pressure = 0
Symmetry Axis	$\mathbf{V_y} = 0$
Wall-blood Interface	$\mathbf{V_y} = 0$ (non-porous wall condition)
	$\mathbf{V_x} = 0$ (no-slip condition)

it was decided to make this inlet velocity a fully developed Poiseuille flow, as detailed in Table 2.1.

2.4.4 Computational Solver

ANSYS Fluent was used to solve the governing cardiovascular equations because of the commercial software's robust and accurate solvers. This choice of commercial software agrees with most modern literature on performing cardiovascular CFD simulations [23; 27]. A 2-D, double precision solver was used with the pressure-velocity coupling SIMPLE algorithm [33]. The Presto! algorithm was used as a pressure solver as it is well suited for high pressure gradient flows, such as those that exist near a strut. Furthermore, the under relaxation factors were set at .3 for pressure and .7 for momentum to ensure quick and accurate convergence, as in [27]. Second-order upwind schemes were used for momentum, turbulent kinetic energy, and the dissipation rate to provide superior accuracy. However, the transient formulation was solved using a first order implicit scheme to offset the computational cost. The time-step was set at .005 seconds as it was found to satisfactorily balance accuracy and computational cost. Special care was taken to ensure that the Courant number remained below one in all simulations as [16] indicates that it is

a necessary condition for simulation accuracy. Additionally, to ensure cyclic convergence, the number of time steps was set to 550 so as to simulate 6 consecutive cardiac cycles.

2.5 Model Validation

Verification of this computational model was performed in three distinct ways. First, it was necessary to prove the model independent of the relevant grid discretizations (spatial, time, and cyclic). The model was then further qualitatively validated against past experimental data and an analytical solution of a simplified geometry.

2.5.1 Grid Independence

Mesh convergence analyses were performed to prove that the solution depended only on physical factors and not on grid discretization. Additionally, these analyses were conducted to ascertain what grid resolution ought to be used in the simulations to balance accuracy and computational time. As this cardiovascular CFD simulation was transient and pulsatile, it was necessary to perform time-step and cyclic convergence analyses as well as the typical spatial mesh convergence. The mesh convergence was judged using the WSS evaluated at two points A and B, where A was directly after the second strut width and B was in the center of the subsequent strut spacing. Points A and B are shown on the model stent geometry of Figure 2.8. Mesh convergence was analyzed by measuring the change in WSS from the previous simulation as the mesh was refined, and successful convergence indicated by the change in WSS declining to zero. This mesh convergence was performed for the base stent geometry depicted in Figure 2.1, where strut width (w) = .08 mm, strut height (h) = .25 mm, and strut spacing (l) = 2 mm, as it was taken to represent all other geometrical variations. Additionally, this mesh convergence analysis was performed with all relevant physical models detailed in section 2.3. As these simulations were transient in nature, the WSS values were measured only during the last velocity peak.

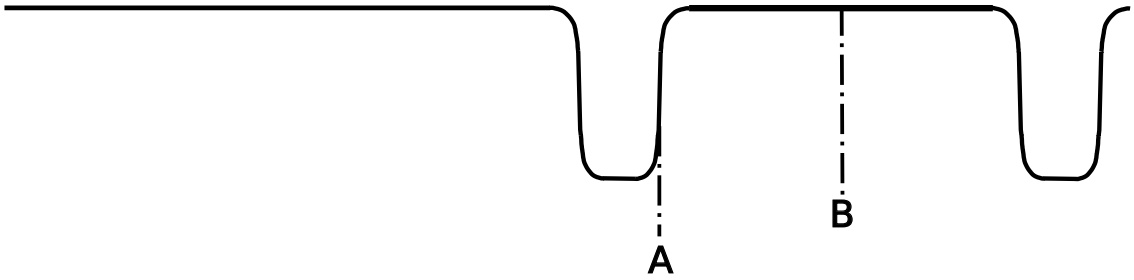

Figure 2.8: Points A and B where the WSS was evaluated to indicate spatial, temporal, and cyclic mesh convergence.

Spatial Mesh Convergence

Spatial mesh convergence analyses were used to select a suitably refined computational mesh while limiting solution time. The coarsest mesh was set at .05 mm sized elements with n representing the corresponding number of elements of this coarsest mesh; this mesh was then progressively refined by doubling the amount of elements of the previous simulation. Spatial mesh convergence, while still being computationally feasible, was achieved at $8n$ (23,216) elements.

Time-step Convergence

The time-step resolution was also refined to prove model independence of the time-step value. This time-step convergence was also performed for the base stent geometry, but now with a spatial mesh of $4n$ resolution. Furthermore, convergence was analyzed only at point B, as point A was numerically sensitive to transient WSS values due to the pulsatile nature of the flow. The initial time-step was set to .01 seconds for a 1 second cardiac cycle with t representing the number of time-steps evaluated for this discretization. The time-step was refined by progressively increasing t tenfold, and the time-step convergence again measured by the change in WSS at each new simulation. This change

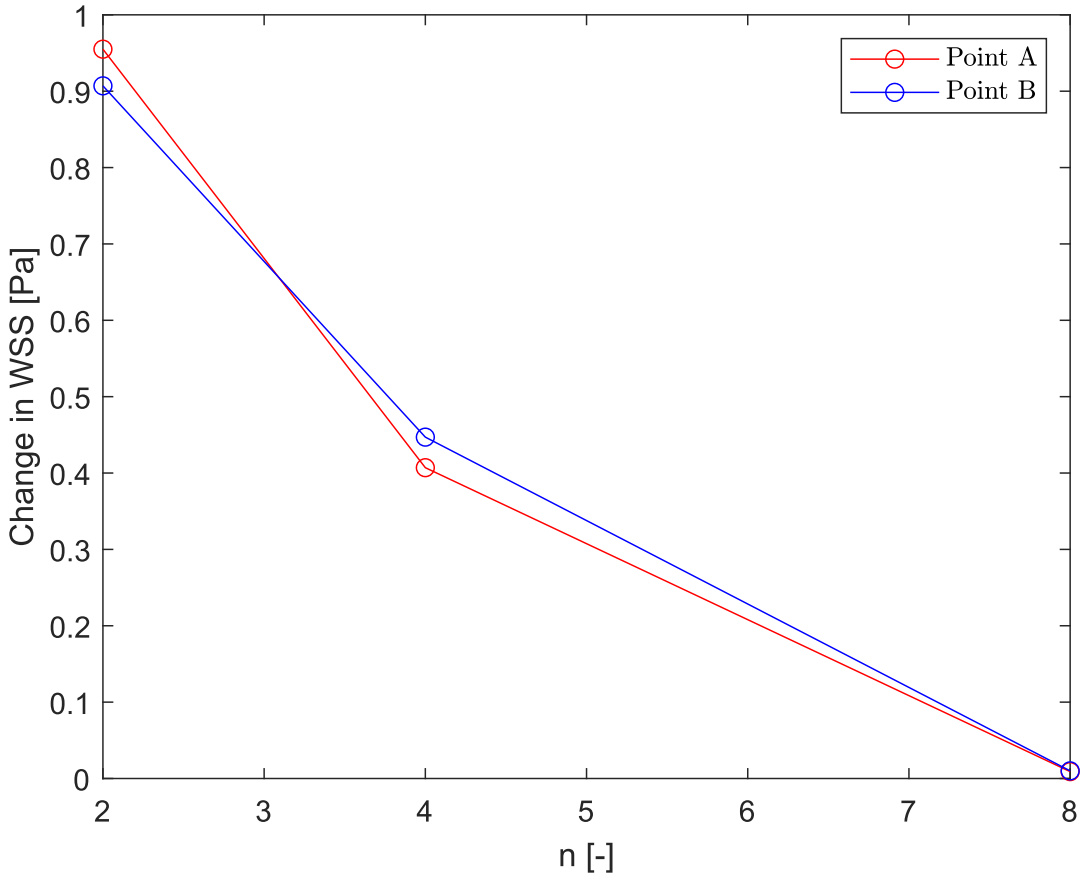

Figure 2.9: Spatial mesh convergence analyzed by progressively refining the spatial mesh from n initial elements. The change in WSS decayed to 0 for a mesh of $8n$ (23,216) elements indicating spatial mesh convergence.

in WSS due to the time-step refinement is shown in Figure 2.10. Achievable time-step convergence was seen at $100t$ before the simulations became unwieldy.

Cyclic Convergence

Finally, it was necessary to prove the model's cyclic independence. Using the aforementioned spatial and temporal mesh discretizations, a simulation was ran on the base stent model simply repeating the number of simulated cardiac cycles. Again, the change in WSS at points A and B was measured after each new cycle until the cycles no longer differed. The cyclic convergence shown in Figure 2.11 indicated that two subsequent cy-

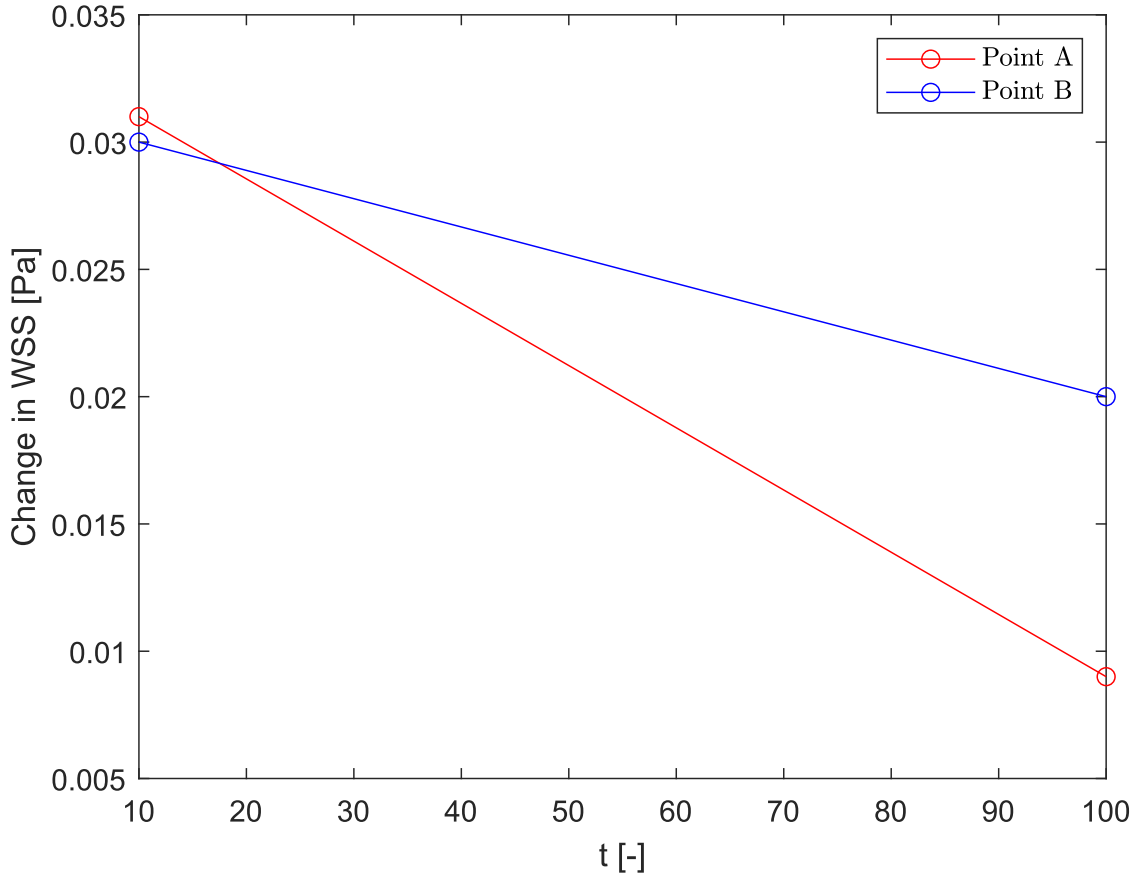

Figure 2.10: Time-step convergence analyzed by progressively refining the time-step from t initial number of time steps. The change in WSS decayed to a negligible .02 Pa for point B by $100t$, though still indicating the proper decay curve for grid independence, before the simulations became too computationally arduous.

cles (and thus three total cycles) were necessary for complete convergence. This rapid convergence, when compared to other research such as [27], was likely due to the newly implemented fully developed, transient, and pulsatile inlet waveform.

2.5.2 Comparison to Other Research

To further justify the validity of the CFD model it was necessary to compare the simulation results against past literature. While it was not possible to exactly replicate a past computational experiment, it was possible to simulate a similar square strut simulation

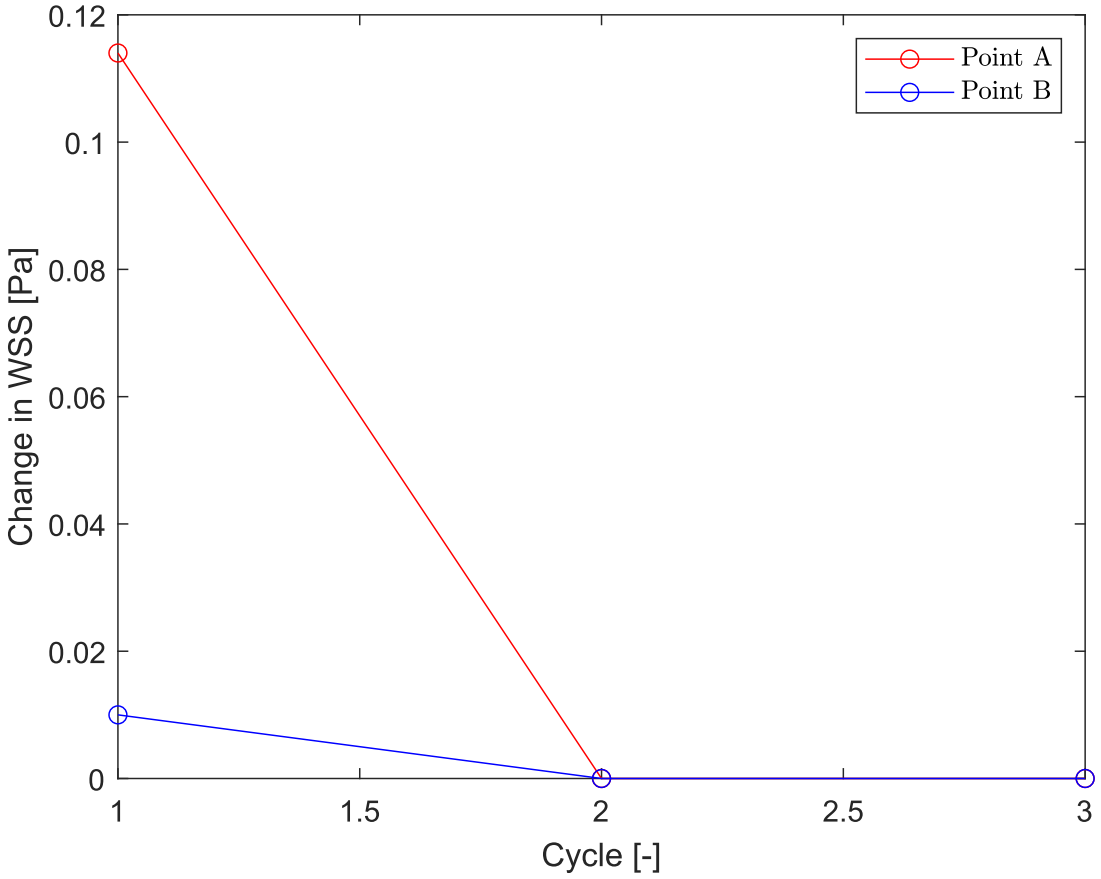

Figure 2.11: Cyclic convergence analyzed by measuring the change in WSS at points A and B for subsequent cycles after the first cardiac cycle (cycle 0). Results indicated that two subsequent cycles (three total cycles) were necessary for cyclic convergence.

to compare qualitative behavior. Past literature was plotted alongside the new simulation results for a square strut in Figure 2.12, and the models demonstrate satisfactory qualitative agreement. It should be noted that while the previous experiment plotted several strut shapes, it is the square strut result (the curve with the lowest WSS) that was used for comparison. Furthermore, the WSS generated by the implemented computational model was presented in a dimensionless form, where Dimensionless WSS $= \frac{\text{WSS}}{\text{Physiological WSS}}$, so as to better compare the qualitative behavior of models built for different conditions.

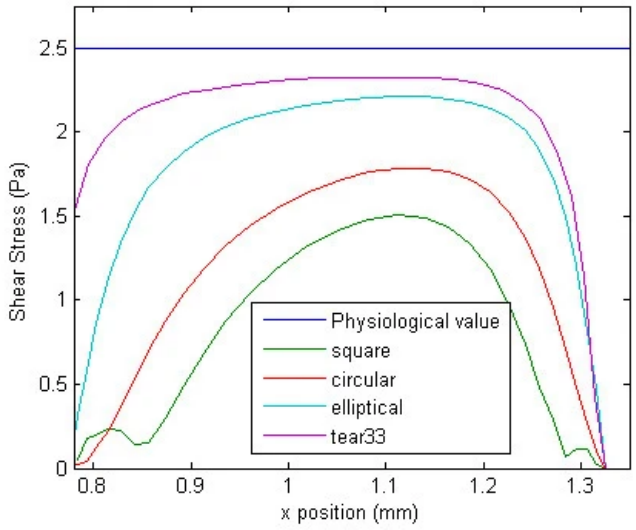

(a) Past simulation results taken from [23].

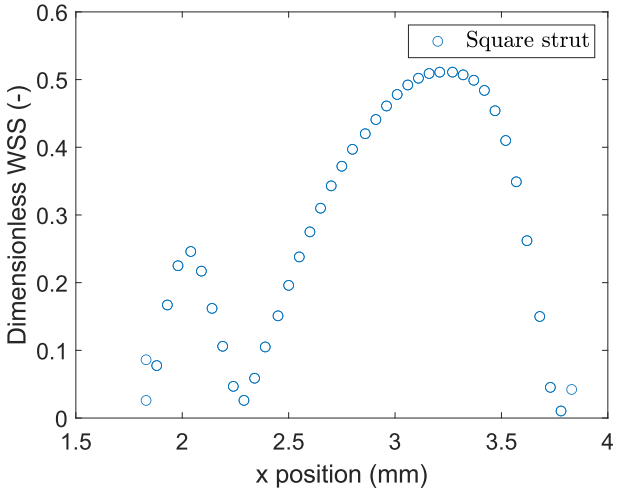

(b) Implemented computational model results for a similar square strut.

Figure 2.12: (a) The WSS profile between the first and second stent struts for various strut shapes. The square strut WSS curve (the curve with the lowest average WSS) was used to validate the implemented computational model. (b) Dimensionless WSS (nondimensionalized by the model's physiological WSS) between the first and second stent struts for a square strut used as comparison to the result in (a). One may note the similar dip and recovery of WSS after the first stent strut (start of the x domain) before the flow is again perturbed by the second stent strut (end of the x domain). This qualitative WSS profile agreement was used to help validate the computational model implemented in this thesis.

2.5.3 Comparison to an Analytical Solution

The computational model was further validated using the analytical two-dimensional version of Poiseuille flow. Poiseuille flow describes describes the flow in a long, narrow cylinder for a viscous, laminar, Newtonian flow. This flow is often used to validate two-dimensional cardiovascular models as it contains similar assumptions to those used to construct computational models [7; 30]. Correspondingly, the computational model implemented in this thesis reduced its assumptions to match those used in the analytical solution to avoid misleading discrepancies.

A two-dimensional, plain arterial geometry (equivalent to an axisymmetric cylinder) was constructed with the same fully developed inlet velocity condition described in section 2.4.3. The arterial dimensions were unchanged and the velocity profile $\mathbf{V_x}$ was inspected at the arterial midpoint ($x = 9$ mm). Substituting the relevant flow parameters into the general analytical solution, presented in full in [46], yields the following expression:

$$\mathbf{V}_{\text{x,exact}} = .265 - .0865y^2 \tag{2.10}$$

where $\mathbf{V}_{\text{x,exact}}$ represents the fully developed x-component of the flow velocity in $\frac{\text{m}}{\text{s}}$ and y represents the distance from the cylinder's center axis in mm.

The analytical and computational model solutions plotted together in Figure 2.13 demonstrated superb agreement, and thus further validated the use of the implemented computational model.

2.6 Statistical Tools

To analyze the hemodynamic performance of the various stents it was decided to employ novel statistical tools. As mentioned in section 1.2.5, the statistical tools used to characterize the risk of in-stent restenosis included a dimensionless mean, coefficient of

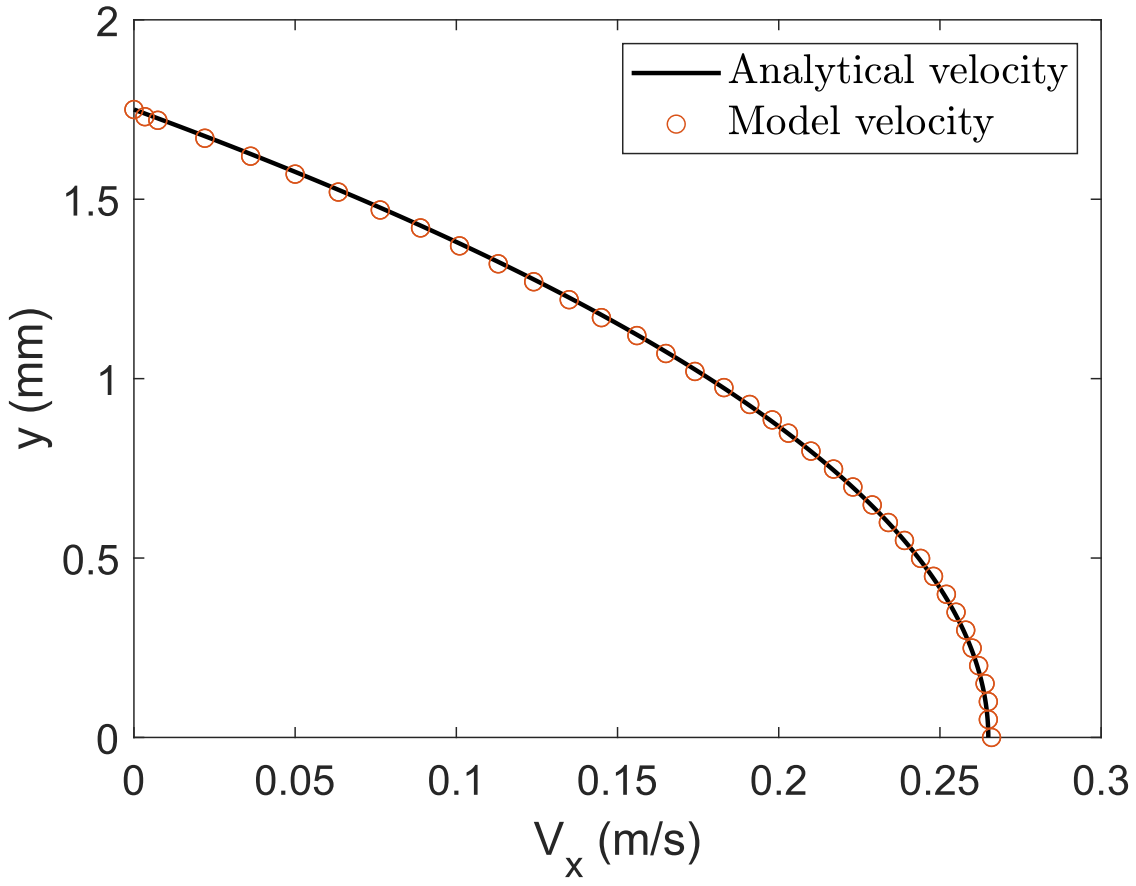

Figure 2.13: Analytical and computational comparison of the solution for the velocity profile in a two dimensional plain cylinder.

variation, and kurtosis coefficient describing the WSS profile. A higher dimensionless mean, lower coefficient of variation, and higher kurtosis coefficient were used to indicate a lower risk of in-stent restenosis. The spatial WSS parameters were taken in the second intra-strut area to facilitate comparisons to past research. These statistical parameters were also compared against the traditional method of characterizing the risk of in-stent restenosis by measuring arterial area under .5 Pa (hereby referred to as the traditional risk of restenosis), also in the second intra-strut area. The WSS profile was only analyzed in this second intra-strut area as there was no significant difference between the subsequent intra-strut zones. Streamline deflection was newly characterized by dividing the temporally and spatially averaged streamline transverse (y-axis) deflection by the artery diame-

ter at all points in the longitudinal direction (x-axis). As the nanovesicles drug technology outlined in section 1.2.2 performs best when there is minimal streamline deflection, it was desired for the stented design to minimize this streamline deflection parameter. Both the WSS and streamline deflection parameters were analyzed in the fourth cycle at the maximum (at 3.234 seconds) and minimum (at 3.734 seconds) inlet velocities, as seen in Figure 2.7, and then temporally averaged to analyze the deflection after cyclic convergence had been achieved.

Chapter 3

Two-Dimensional Model Results

3.1 Overview

The results from the two-dimensional models concerned the WSS and average streamline deflection of the changing geometrical features illustrated in section 2.4.1 as well as quantifying the effect of the physical models mentioned in section 2.3. The results are first presented using the statistical methods outlined in 2.6 and then discussed in a subsequent section.

3.2 Benchmark Results

It was first necessary to create two benchmark stent models, both to compare against past literature as seen in section 2.5.2 and to contextualize the various numerical results. The first benchmark model was constructed using rectangular struts with $w = .08$ mm, $h = .25$ mm, and $l = 2$ mm with all active modelling assumptions and was used to analyze the effect of changing the physical model. The second benchmark model was simply the first benchmark model but with $h = .08$ mm, and was the model upon which all geometrical simulations were compared as it was more accurate of modern stent parameter

values. This second benchmark model was the same as the final strut height simulation, and was included in Table 3.1 alongside the first benchmark model.

Table 3.1: Statistical WSS and streamline deflection results for the benchmark stent models.

	Dimensionless Mean (-)	Traditional risk of restenosis (%)	Coefficient of variation (-)	Kurtosis coefficient (-)	Dimensionless streamline deflection (-)
Benchmark 1	0.295	34.7	0.829	5.43	0.260
Benchmark 2	0.535	10.4	0.395	6.18	0.262

3.3 Streamlined Cross-Sectional Profile Results

The various streamlined cross-sectional profiles analyzed were fillets and conic struts and they were compared to the second benchmark model. Three different fillet configurations (top, bottom, and combined) were analyzed while the conic profiles ranged from a flattened ellipse to a triangular hyperbolic strut based on the conic ρ value.

3.3.1 Fillet Configurations

As described in section 2.4.1, three configurations of fillets were tested while varying the dimensionless fillet strength in each simulation. Again, the top fillet represents a chemically polished streamlined profile while the bottom fillet represents the profile formed by the re-endothelialization of an embedded strut. At maximum fillet strength, these configurations resulted in a complete reshaping of the strut into a circular one. The aforementioned statistical tools used to quantify WSS and streamline deflection were calculated for each geometrical configuration and listed in Tables 3.2, 3.3, and 3.4 for the bottom, top, and combined fillet configurations, respectively.

Table 3.2: Statistical WSS and streamline deflection results as fillet strength was varied for the bottom fillet configuration.

Fillet Strength	Dimensionless Mean (-)	Traditional risk of restenosis (%)	Coefficient of variation (-)	Kurtosis coefficient (-)	Dimensionless streamline deflection (-)
.2	0.483	28.4	0.645	1.50	0.268
.4	0.518	23.1	0.545	1.56	0.264
.6	0.557	16.4	0.462	2.27	0.264
.8	0.571	14.7	0.428	1.56	0.264
1.0	0.583	12.5	0.384	1.94	0.264

Table 3.3: Statistical WSS and streamline deflection results as fillet strength was varied for the top fillet configuration.

Fillet Strength	Dimensionless Mean (-)	Traditional risk of restenosis (%)	Coefficient of variation (-)	Kurtosis coefficient (-)	Dimensionless streamline deflection (-)
.2	0.600	12.8	0.390	1.96	0.274
.4	0.629	10.2	0.338	2.70	0.264
.6	0.640	7.03	0.303	3.52	0.262
.8	0.628	4.91	0.255	4.74	0.263
1.0	0.656	4.16	0.232	6.05	0.264

3.3.2 Conic Profiles

The conic profiles were characterized by their conic ρ value which was varied between a flattened elliptical cross-sectional profile ($\rho = .05$) and a near triangular cross-sectional profile ($\rho = .925$). However, the maximum strut height was maintained at $h = .08$ mm, as described by the second benchmark model, in order to better separate the effects of a streamlined profile and a changing strut height. Conic WSS and streamline deflection results are listed in Table 3.5.

Table 3.4: Statistical WSS and streamline deflection results as fillet strength was varied for the combined fillet configuration.

Fillet Strength	Dimensionless Mean (-)	Traditional risk of restenosis (%)	Coefficient of variation (-)	Kurtosis coefficient (-)	Dimensionless streamline deflection (-)
.2	0.458	31.1	0.636	0.638	0.264
.6	0.534	17.2	0.440	1.43	0.263
1.0	0.508	8.58	0.323	2.54	0.262

Table 3.5: Statistical WSS and streamline deflection results for the various conic strut cross-sectional profiles.

Conic rho	Dimensionless Mean (-)	Traditional risk of restenosis (%)	Coefficient of variation (-)	Kurtosis coefficient (-)	Dimensionless streamline deflection (-)
0.050	0.493	8.71	0.308	2.28	0.260
0.341	0.497	9.09	0.322	2.47	0.260
0.633	0.501	7.69	0.302	2.77	0.260
0.925	0.543	7.57	0.302	3.04	0.261

3.4 Strut Taper Results

The CFD results for the varying strut taper angle were compiled into Table 3.6 and represent an extension of the FEA research introduced in section 1.2.3.

Table 3.6: Statistical WSS and streamline deflection results as θ was varied for the tapered stents.

theta	Dimensionless Mean (-)	Traditional risk of restenosis (%)	Coefficient of variation (-)	Kurtosis coefficient (-)	Dimensionless streamline deflection (-)
1.5	0.427	25.9	0.671	1.67	0.261
3.0	0.435	24.4	0.638	1.33	0.262
4.5	0.470	23.6	0.637	1.06	0.262

3.5 Stent Mechanical Parameter Results

This section concerns those mechanical stent parameters most often analyzed in cardiovascular CFD research: strut width, strut height, and strut spacing. However, these presented results were conducted with a more complex blood model as described in section 2.3. The relevant flow parameters were compared against varying mechanical parameters based on the second benchmark model, while holding the other parameters constant. Tables 3.7, 3.8, and 3.9 describe the results for changing strut widths, heights, and spacing, respectively.

Table 3.7: Statistical WSS and streamline deflection results for a changing strut width.

Strut Width (mm)	Dimensionless Mean (-)	Traditional risk of restenosis (%)	Coefficient of variation (-)	Kurtosis coefficient (-)	Dimensionless streamline deflection (-)
0.25	0.569	14.2	0.441	2.50	0.264
0.2	0.565	12.1	0.418	2.88	0.264
0.15	0.568	10.7	0.400	3.47	0.268
0.10	0.529	10.8	0.363	3.07	0.268

Table 3.8: Statistical WSS and streamline deflection results for a changing strut height.

Strut Height (mm)	Dimensionless Mean (-)	Traditional risk of restenosis (%)	Coefficient of variation (-)	Kurtosis coefficient (-)	Dimensionless streamline deflection (-)
0.2	0.363	25.3	0.737	6.54	0.280
0.15	0.417	21.0	0.585	5.88	0.274
0.1	0.499	11.9	0.443	6.75	0.269
0.08	0.535	10.4	0.395	6.18	0.262

3.6 The Effect of the Various Blood Models

The effect of the various blood models was analyzed using the same WSS and streamline deflection statistical tools used in the other simulations. Five different models – with

Table 3.9: Statistical WSS and streamline deflection results for a changing strut spacing.

Strut Spacing (mm)	Dimensionless Mean (-)	Traditional risk of restenosis (%)	Coefficient of variation (-)	Kurtosis coefficient (-)	Dimensionless streamline deflection (-)
1.75	0.540	11.4	0.487	4.18	0.263
2.25	0.572	12.8	0.445	3.50	0.262
2.5	0.588	11.4	0.460	3.74	0.261
2.75	0.569	12.1	0.466	3.93	0.261

the base model representing the simplest laminar, Newtonian, and steady blood flow model – and their statistical parameters are described in Table 3.10.

Table 3.10: Statistical WSS and streamline deflection results for physical modelling variations on the first benchmark model, with the transient model evaluated at the same inlet velocity as the other models (at 3.234 seconds).

Blood model	Dimensionless Mean (-)	Traditional risk of restenosis (%)	Coefficient of variation (-)	Kurtosis coefficient (-)	Dimensionless streamline deflection (-)
Base model	0.154	67.1	1.02	21.3	0.298
Non-Newtonian	0.349	28.7	0.561	2.77	0.271
Transient	0.217	50.0	1.05	5.52	0.321
$k-\epsilon$	0.202	50.5	0.932	31.3	0.286
SST $k-\omega$	0.151	68.0	1.01	28.5	0.296

3.7 Discussion of Results

The results of sections 3.2-3.6 are here briefly commented upon. The results were contextualized for both general desired stent performance as well as for specific application to nanovesicle based drug delivery.

However, it was first necessary to evaluate the different WSS statistical parameters to ascertain those which were most useful. The introduced dimensionless mean, coefficient of variation, and kurtosis coefficient typically exhibited the correct trends (as illus-

trated by the traditional risk of restenosis method) in characterizing the hemodynamics of stent performance. The coefficient of variation and kurtosis coefficient, particularly, introduced useful, novel ways of understanding the WSS profile. The dimensionless mean, however, sought to represent a similar characterization of the WSS profile as the traditional risk method. While the dimensionless mean typically exhibited the correct trend, it was more sensitive to numerical changes in the model. This sensitivity was likely due in part to the dimensionless mean being increasingly susceptible to points of high WSS being transported off the struts themselves, often due to the pulsatile nature of the flow. This transient flow susceptibility was likely the cause of the incorrect dimensionless mean trend seen in Table 3.7. Hence, it was decided to primarily use the traditional method of measuring the risk of restenosis instead of the dimensionless mean for these pulsatile simulations; though, the coefficient of variation and kurtosis coefficient were still used to visualize the WSS profile.

3.7.1 Streamlined Cross-Sectional Profile Discussion

To better clarify the streamlined cross-sectional profile results, the tabulated data in Tables 3.2-3.5 were collected into Figures 3.1-3.2, respectively concerning the fillet and conic profile results. Additionally, the fillet configurations were only plotted against the traditional risk of restenosis (%) as it was deemed the more robust WSS tool, while the streamline deflection parameter was not plotted as it demonstrated an insignificant change of less than 5% in all models.

From Tables 3.2-3.4, one may note that the fillet configuration negligibly affected the dimensionless streamline deflection parameter with a maximum difference of less than 1% at full fillet strength. However, each fillet demonstrated the same trend of a decreasing streamline deflection parameter as fillet strength increased. For example, across the range of fillet strengths, the top fillet configuration exhibited the most drastic effect on the deflection parameter at 3.7%. The conic profiles demonstrated a far less significant change in the parameter across the analyzed range.

More interesting was the effect of the streamlined profiles on the WSS profile. All streamlined profiles demonstrated significant differences along their analyzed range, though the conic profiles only deviated by 18% while the top fillet configuration varied by around 100%. Interestingly, it was the top fillet configuration which demonstrated the best hemodynamic WSS performance at maximum fillet strength, improving upon the second benchmark model by 85%. Thus, streamlining cross-sectional profiles was deemed imperative for improving stent hemodynamic performance and ought to be considered in any design study. An interesting anomaly was the bottom fillet as it performed worse than the benchmark model at all fillet strengths. The bottom fillet introduced material (due to endothelialization) to create its streamline, and it was likely this introduced material that proved more significant than the streamlining it introduced. Thus, the streamlined profile formed due to endothelialization was seen to negatively impact the hemodynamics. This same phenomenon was also seen in the combined fillet configuration, though it was offset by the better performing bottom fillet. Additionally, the validity and significance of these results was furthered by the encouraging monotonic trend of the results. Increasing fillet strength was largely seen to improve the hemodynamics, supporting the use of circular fillet struts in future designs.

Unfortunately, there was no clear trend for the conic profiles. While the conic profiles consistently performed better than the second benchmark model, the hemodynamic performance did not change monotonically with respect to the conic ρ. Hence, it was proposed that more data points were necessary to truly characterize the effect of the conic ρ and to ascertain whether the trend was simply affected by a numerical outlier.

3.7.2 Strut Taper Discussion

Tapering the stent profile negligibly impacted the streamline deflection while monotonically affecting the WSS profile. The tapered strut profiles described in Table 3.6 exhibited a consistent trend of decreasing risk of restenosis for increased strut taper, reaching a maximum difference of 9.2%. This result was chiefly significant as it supported the use of

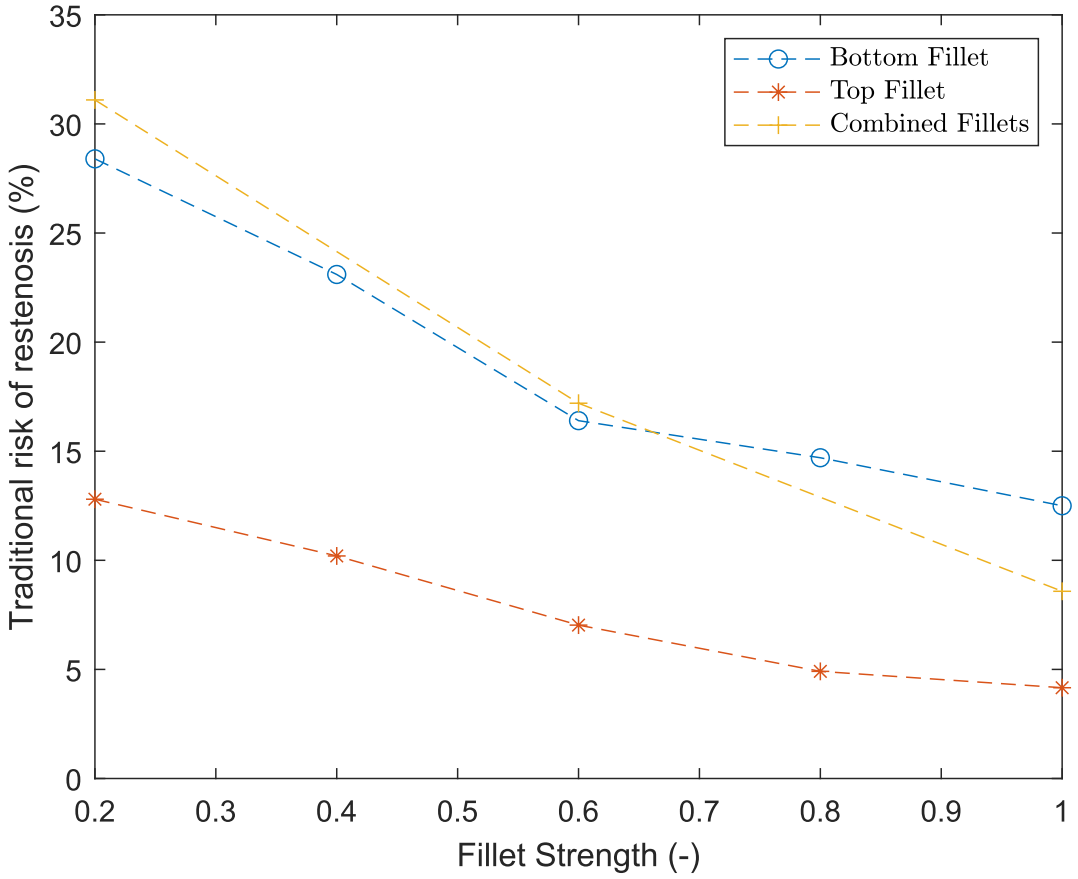

Figure 3.1: The effect of the various fillet configurations, and fillet strength, on the traditional risk of restenosis quantified by the percentage of arterial area under .5 Pa in the second intra-strut area.

tapered stent connectors in future stent design. It should be noted that this result was not compared against the second benchmark model as the strut taper represents the tapering along a stent connector, and is thus not comparable to the behavior in the intra-strut area.

3.7.3 Stent Mechanical Parameter Discussion

The three traditional stent mechanical parameters were plotted together to clarify their relative importance. First, the effect on the traditional WSS metric was plotted in Figure 3.3. Next, the streamline deflection results were plotted in Figure 3.4 as the strut height was found to be particularly influential.

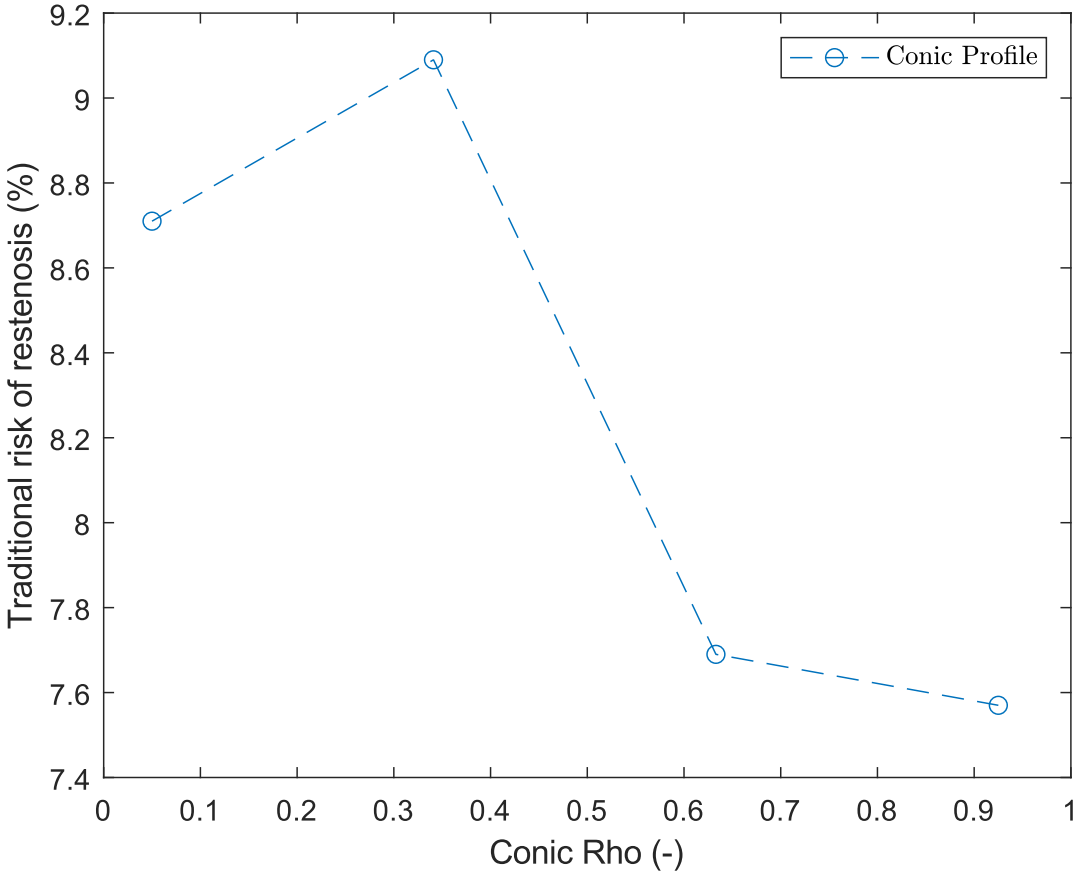

Figure 3.2: The effect of changing the conic ρ defining the cross-sectional profile on the traditional risk of restenosis quantified by the percentage of arterial area under .5 Pa in the second intra-strut area.

The results of these mechanical parameters indicated that previous literature using more simplified blood models is still valid, at least qualitatively. Particularly, strut height exhibited the largely monotonic improvement trend for both WSS and streamline deflection as expected. Additionally, it was reaffirmed that strut height was the most significant parameter for both WSS and streamline deflection. In fact, a changing strut height was the only parameter to notably affect the streamline deflection parameter with a 6.6% deflection parameter range within the analyzed interval. The strut width was significant only for the WSS profile, but, again, exhibited a lesser effect than strut height. Curiously, the strut width also demonstrated signs of thresholding for streamline deflection, indicating

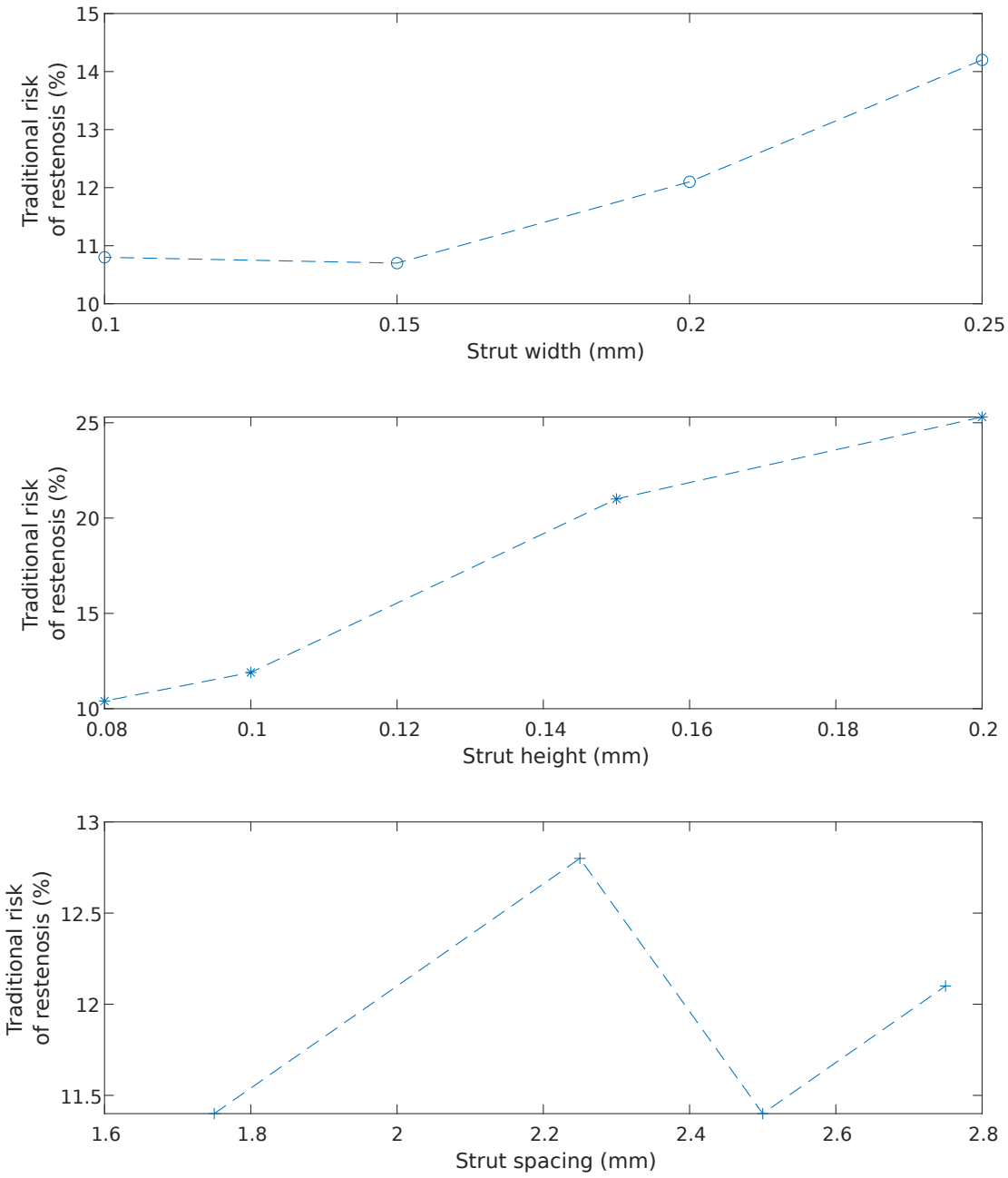

Figure 3.3: The effect of the various traditional mechanical parameters on the traditional risk of restenosis. From top to bottom, the mechanical parameter of interest was: strut width, strut height, and strut spacing.

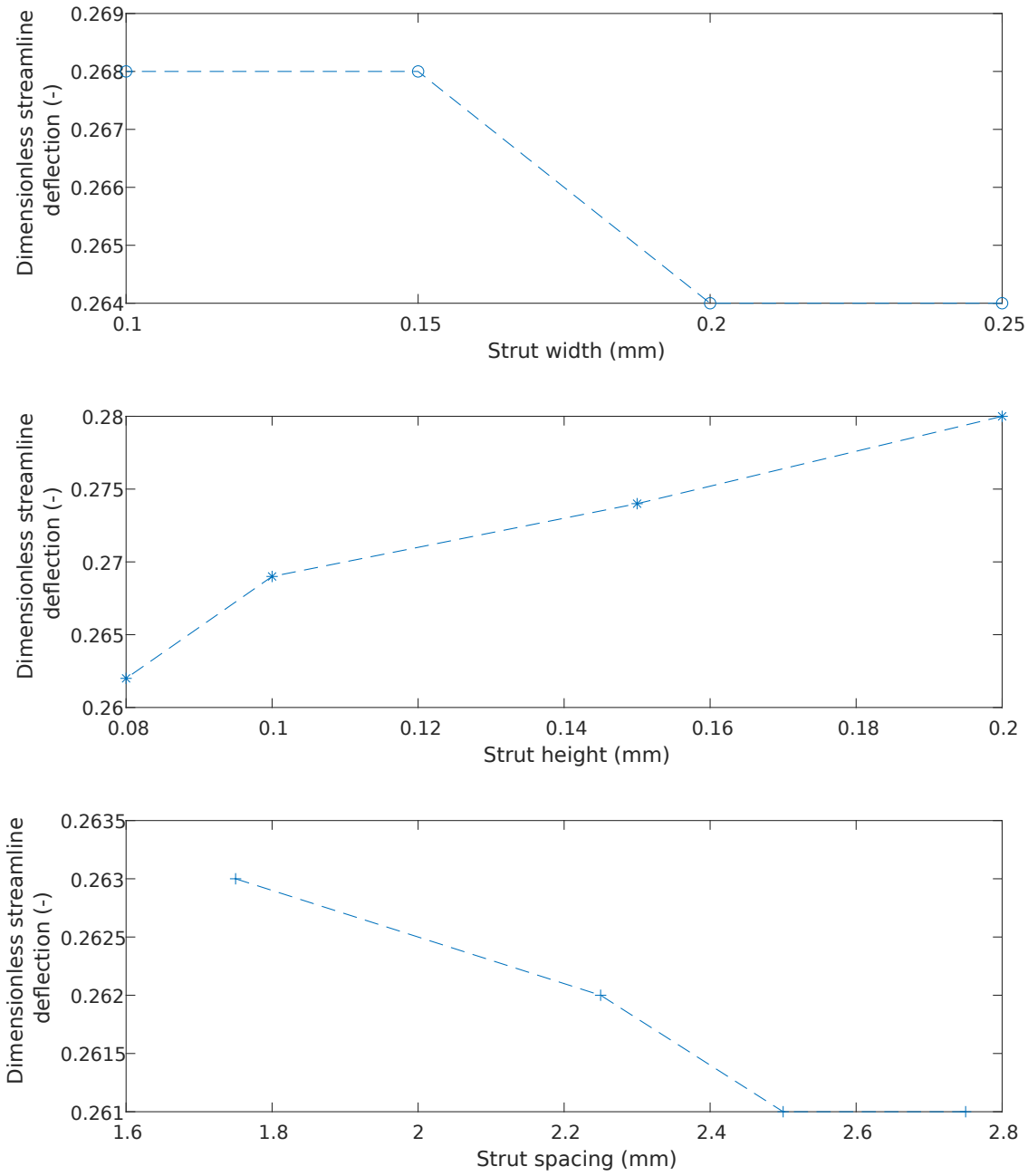

Figure 3.4: The effect of the various traditional mechanical parameters on the dimensionless streamline deflection parameter. From top to bottom, the mechanical parameter of interest was: strut width, strut height, and strut spacing.

that there were special physical phenomena occurring around the analyzed range. On the other hand, strut spacing demonstrated no significant effect on either WSS or streamline deflection, likely indicating that the analyzed range was too small as the dimensions were sufficiently long for the parameter to become negligible. This was represented by the lack of a coherent strut spacing trend, as it seemed the statistical parameters had become somewhat independent of the strut spacing. This strut spacing result supported a phenomenon seen in the other results where the stent hemodynamic performance indicated diminishing returns for changing stent parameters.

3.7.4 Discussion of the Various Blood Models

The choice of blood model significantly affected the WSS and streamline deflection results described in Table 3.10. Furthermore, the most significant assumption, as expected, was taking blood to be Newtonian. The non-Newtonian model demonstrated an 80% relative difference in restenosis risk and 9.5% difference in streamline deflection compared to the simplest model. This result indicated that it is significantly incorrect to take blood to be Newtonian even for coronary artery flow. When compared to the first benchmark model (the complex blood model used in the simulations), this non-Newtonian model still demonstrated a 19% and 4.1% error for WSS and streamline deflection. This residual error was likely due to the transient assumption which also demonstrated a significant effect on WSS and streamline deflection. The non-Newtonian and transient models did not just change the quantitative results, they introduced new physics that need to be properly modelled. Thus, it was proposed that the only assumption which may be safely omitted was taking blood to be in a laminar flow regime. As described in section 2.3.2, the SST $k-\omega$ is typically viewed as the more accurate turbulent blood model, and here it negligibly affected the results.

Chapter 4

Final Conclusions and Summary

4.1 Limitations and Recommendations

Possibly the greatest limitation of this research was the lack of supporting clinical human or animal cardiovascular data due to the expensive and time costly nature of these experiments. However, more relevant were the numerical limitations of the performed cardiovascular simulations. Blood was taken to be a homogeneous mixture for numerical simplicity, but past research indicates that it is perhaps necessary to model the aggregation of cells in flow stagnation zones, and this phenomenon ought to be considered in future research. Additionally, one ought to consider the mechanics of red blood cell and platelet collision with stent surfaces, as it may affect stent hemodynamics. This research was also performed solely in two-dimensions due to the computational cost of simulating a transient, three-dimensional geometry. While this simplification is typically acceptable for comparative hemodynamic studies, it would nonetheless be an improvement to more accurately represent the true model geometry. Furthermore, when conducting a three-dimensional study, it is advised to use patient accurate geometries, as the conducted research indicated that stent hemodynamic performance is quite sensitive to small changes in geometry.

4.2 Summary

Various stent geometrical design features were analyzed using a complex, two-dimensional blood model for a simplified coronary artery geometry. Results supported the use of complex blood models while illuminating the allowable simplifications, such as ignoring turbulence, that may be made with little error. Additionally, the utilization of this complex blood model supported the work of previous authors in simulating stent mechanical parameters with more simplified models. Though, modelling blood as a non-Newtonian, transient fluid was deemed crucial for characterising the hemodynamics accurately. Nonetheless, strut height was confirmed in its hemodynamic importance for both WSS and streamline deflection. Finally, the chief work of this thesis indicated that it was the circular cross section – defined by a maximum circular fillet radius – that was the most effective of the streamlined cross-sectional profiles. Furthermore, this cross-sectional profile exhibited a significant improvement upon less streamlined profiles in terms of WSS. Hence, streamlining stent strut cross-sectional profiles ought always be considered in stent design due to the notable improvement in hemodynamic performance. However, no cross-sectional profile succeeded in notably decreasing the streamline deflection. In fact, the only geometrical feature to significantly improve the streamline deflection was the strut height. Thus, stent design concerning nanovesicle based treatments ought to particularly concern itself with minimizing stent strut height.

Bibliography

[1] Erling Falk. Pathogenesis of atherosclerosis. *Journal of the American College of Cardiology*, 47(8_Supplement):C7–C12, 2006. doi: 10.1016/j.jacc.2005.09.068.

[2] Timothy Watson, Mark W I Webster, John A Ormiston, Peter N Ruygrok, and James T Stewart. Long and short of optimal stent design. *Open Heart*, 4(2):e000680, 2017.

[3] Hiroyuki Jinnouchi, Sho Torii, Atsushi Sakamoto, Frank D. Kolodgie, Renu Virmani, and Aloke V. Finn. Fully bioresorbable vascular scaffolds: lessons learned and future directions. *Nature Reviews Cardiology*, 16(5):286–304, 2019.

[4] Hao-Ming Hsiao, Chien-Han Lin, Ying-Chih Liao, Hsien-Yeh Chen, and Tzu-Wei Wang. Hemodynamic behavior of coronary stents in straight and curved arteries. *Current Nanoscience*, 10:205–211, 04 2014.

[5] Juan M. Jiménez and Peter F. Davies. Hemodynamically driven stent strut design. *Annals of Biomedical Engineering*, 37(8):1483–1494, 2009.

[6] Blouza Adel, Laurent Dumas, and Ibrahima M'Baye. *Multiobjective optimization of a stent in a fluid-structure context*. 2008.

[7] Bulman-Fleming. *Numerical simulations of stent-based local drug delivery : 2D geometric investigations and the evaluation of 3D designs on the basis of local delivery effectiveness*. Thesis, McGill University, 2003.

[8] J. J. Boyle. Macrophage activation in atherosclerosis: Pathogenesis and pharmacology of plaque rupture. *Current Vascular Pharmacology*, 3(1):63–68, 2005.

[9] Neil J. Stone. The clinical and economic significance of atherosclerosis. *The American Journal of Medicine*, 101(4, Supplement 1):6S–9S, 1996.

[10] O. Kobo, M. Saada, S. R. Meisel, E. Hellou, A. Frimerman, R. A. Fanne, J. Mohsen, A. Danon, and A. Roguin. Modern stents: Where are we going? *Rambam Maimonides Med J*, 11(2), 2020. 2076-9172 Kobo, Ofer Saada, Majdi Meisel, Simcha R Hellou, Elias Frimerman, Aaron Fanne, Rami Abu Mohsen, Jameel Danon, Asaf Roguin, Ariel Journal Article Review 2020/05/07 Rambam Maimonides Med J. 2020 Apr 29;11(2):e0017. doi: 10.5041/RMMJ.10403.

[11] J. Mejia, R. Mongrain, and O. F. Bertrand. Accurate prediction of wall shear stress in a stented artery: newtonian versus non-newtonian models. *J Biomech Eng*, 133(7):074501, 2011. 1528-8951 Mejia, Juan Mongrain, Rosaire Bertrand, Olivier F Journal Article United States J Biomech Eng. 2011 Jul;133(7):074501. doi: 10.1115/1.4004408.

[12] A. Kastrati, J. Dirschinger, P. Boekstegers, S. Elezi, H. Schühlen, J. Pache, G. Steinbeck, C. Schmitt, K. Ulm, F. J. Neumann, and A. Schömig. Influence of stent design on 1-year outcome after coronary stent placement: a randomized comparison of five stent types in 1,147 unselected patients. *Catheter Cardiovasc Interv*, 50(3):290–7, 2000. Kastrati, A Dirschinger, J Boekstegers, P Elezi, S Schühlen, H Pache, J Steinbeck, G Schmitt, C Ulm, K Neumann, F J Schömig, A Clinical Trial Comparative Study Journal Article Multicenter Study Randomized Controlled Trial Research Support, Non-U.S. Gov't United States Catheter Cardiovasc Interv. 2000 Jul;50(3):290-7. doi: 10.1002/1522-726x(200007)50:3<290::aid-ccd5>3.0.co;2-w.

[13] C. Rogers and E. R. Edelman. Endovascular stent design dictates experimental restenosis and thrombosis. *Circulation*, 91(12):2995–3001, 1995. Rogers, C Edelman, E R AG00294/AG/NIA NIH HHS/United States GM/HL49039/GM/NIGMS NIH HHS/United States HL-17747/HL/NHLBI NIH HHS/United States Journal Article

Research Support, Non-U.S. Gov't Research Support, U.S. Gov't, P.H.S. United States Circulation. 1995 Jun 15;91(12):2995-3001. doi: 10.1161/01.cir.91.12.2995.

[14] Jeong-Kee Yoon, Dae-Hyun Kim, Mi-Lan Kang, Hyeon-Ki Jang, Hyun-Ji Park, Jung Bok Lee, Se Won Yi, Hye-Seon Kim, Sewoom Baek, Dan Bi Park, Jin You, Seong-Deok Lee, Yoshitaka Sei, Song Ih Ahn, Young Min Shin, Chang Soo Kim, Sangsu Bae, YongTae Kim, and Hak-Joon Sung. Anti-atherogenic effect of stem cell nanovesicles targeting disturbed flow sites. *Small*, 16(16):2000012, 2020.

[15] Jafar Moradicheghamahi, Jaber Sadeghiseraji, and Mehdi Jahangiri. Numerical solution of the pulsatile, non-newtonian and turbulent blood flow in a patient specific elastic carotid artery. *International Journal of Mechanical Sciences*, 150:393–403, 2019.

[16] T. J. Gundert, A. L. Marsden, W. Yang, and Jr. LaDisa, J. F. Optimization of cardiovascular stent design using computational fluid dynamics. *J Biomech Eng*, 134(1):011002, 2012. 1528-8951 Gundert, Timothy J Marsden, Alison L Yang, Weiguang LaDisa, John F Jr Wellcome Trust/United Kingdom Journal Article Research Support, Non-U.S. Gov't Research Support, U.S. Gov't, Non-P.H.S. United States J Biomech Eng. 2012 Jan;134(1):011002. doi: 10.1115/1.4005542.

[17] John F. LaDisa, Lars E. Olson, Douglas A. Hettrick, David C. Warltier, Judy R. Kersten, and Paul S. Pagel. Axial stent strut angle influences wall shear stress after stent implantation: analysis using 3d computational fluid dynamics models of stent foreshortening. *BioMedical Engineering OnLine*, 4(1):59, 2005.

[18] Yunduo Charles Zhao, Parham Vatankhah, Tiffany Goh, Rhys Michelis, Kiarash Kyanian, Yingqi Zhang, Zhiyong Li, and Lining Arnold Ju. Hemodynamic analysis for stenosis microfluidic model of thrombosis with refined computational fluid dynamics simulation. *Scientific reports*, 11(1):6875–6875, 2021. 33767279[pmid] PMC7994556[pmcid] 10.1038/s41598-021-86310-2[PII].

[19] George C. Kagadis, Eugene D. Skouras, George C. Bourantas, Christakis A. Paraskeva, Konstantinos Katsanos, Dimitris Karnabatidis, and George C. Nikiforidis. Computational representation and hemodynamic characterization of in vivo acquired severe stenotic renal artery geometries using turbulence modeling. *Medical Engineering Physics*, 30(5):647–660, 2008.

[20] Borja Ibañez, Juan J. Badimon, and Mario J. Garcia. Diagnosis of atherosclerosis by imaging. *The American Journal of Medicine*, 122(1, Supplement):S15–S25, 2009. Management of Atherosclerosis: A Practical Guide in 2008.

[21] Blessy Thomas and K.S.Sumam. Blood flow in human arterial system-a review. *Procedia Technology*, 24, 2016.

[22] Longzhen Wang, Junfei Tong, Pengfei Dong, David Wilson, Hiram Bezerra, and Linxia Gu. *Mechanical Performance of PLLA Stent*, volume 2018. Design of Medical Devices Conference, 2018.

[23] Juan Mejia, Bilal Ruzzeh, Rosaire Mongrain, Richard Leask, and Olivier F. Bertrand. Evaluation of the effect of stent strut profile on shear stress distribution using statistical moments. *BioMedical Engineering OnLine*, 8(1):8, 2009.

[24] K. Kolandaivelu, R. Swaminathan, W. J. Gibson, V. B. Kolachalama, K. L. Nguyen-Ehrenreich, V. L. Giddings, L. Coleman, G. K. Wong, and E. R. Edelman. Stent thrombogenicity early in high-risk interventional settings is driven by stent design and deployment and protected by polymer-drug coatings. *Circulation*, 123(13):1400–9, 2011. 1524-4539 Kolandaivelu, Kumaran Swaminathan, Rajesh Gibson, William J Kolachalama, Vijaya B Nguyen-Ehrenreich, Kim-Lien Giddings, Virginia L Coleman, Leslie Wong, Gee K Edelman, Elazer R R01 GM049039/GM/NIGMS NIH HHS/United States R01 GM049039-15/GM/NIGMS NIH HHS/United States R01 GM 49039/GM/NIGMS NIH HHS/United States Comparative Study Journal Arti-

cle Research Support, N.I.H., Extramural Circulation. 2011 Apr 5;123(13):1400-9. doi: 10.1161/CIRCULATIONAHA.110.003210. Epub 2011 Mar 21.

[25] M. Iantorno, M. J. Lipinski, H. M. Garcia-Garcia, B. J. Forrestal, T. Rogers, D. Gajanana, K. D. Buchanan, R. Torguson, W. S. Weintraub, and R. Waksman. Meta-analysis of the impact of strut thickness on outcomes in patients with drug-eluting stents in a coronary artery. *Am J Cardiol*, 122(10):1652–1660, 2018. 1879-1913 Iantorno, Micaela Lipinski, Michael J Garcia-Garcia, Hector M Forrestal, Brian J Rogers, Toby Gajanana, Deepakraj Buchanan, Kyle D Torguson, Rebecca Weintraub, William S Waksman, Ron Journal Article Meta-Analysis Research Support, Non-U.S. Gov't Review United States 2018/10/08 Am J Cardiol. 2018 Nov 15;122(10):1652-1660. doi: 10.1016/j.amjcard.2018.07.040. Epub 2018 Sep 8.

[26] G. Alaimo, F. Auricchio, M. Conti, and M. Zingales. Multi-objective optimization of nitinol stent design. *Medical Engineering Physics*, 47:13–24, 2017.

[27] Yongfei Jiang, Jun Zhang, and Wanhua Zhao. Influence of strut cross-section of stents on local hemodynamics in stented arteries. *Chinese Journal of Mechanical Engineering*, 29(3):624–632, 2016.

[28] A. O. Frank, P. W. Walsh, and Jr. Moore, J. E. Computational fluid dynamics and stent design. *Artif Organs*, 26(7):614–21, 2002. Frank, Andreas O Walsh, Peter W Moore, James E Jr S06 GM08205/GM/NIGMS NIH HHS/United States Journal Article Research Support, U.S. Gov't, P.H.S. Review United States 2002/06/26 Artif Organs. 2002 Jul;26(7):614-21. doi: 10.1046/j.1525-1594.2002.07084.x.

[29] Hannan Tahir, Alfons G. Hoekstra, Eric Lorenz, Patricia V. Lawford, D. Rodney Hose, Julian Gunn, and David J.W. Evans. Multi-scale simulations of the dynamics of in-stent restenosis: impact of stent deployment and design. *Interface Focus*, 1(3):365–373, 2011.

[30] Kristen Karman. 2-D CFD design of the cross-sectional shape of arterial stents. Masters theses and doctoral dissertations, University of Tennessee at Chattanooga, 2013.

[31] J. V. Soulis, G. D. Giannoglou, Y. S. Chatzizisis, K. V. Seralidou, G. E. Parcharidis, and G. E. Louridas. Non-newtonian models for molecular viscosity and wall shear stress in a 3d reconstructed human left coronary artery. *Med Eng Phys*, 30(1):9–19, 2008. Soulis, Johannes V Giannoglou, George D Chatzizisis, Yiannis S Seralidou, Kypriani V Parcharidis, George E Louridas, George E Journal Article England Med Eng Phys. 2008 Jan;30(1):9-19. doi: 10.1016/j.medengphy.2007.02.001. Epub 2007 Apr 6.

[32] D. Lopes, H. Puga, J. Teixeira, and R. Lima. Blood flow simulations in patient-specific geometries of the carotid artery: A systematic review. *Journal of Biomechanics*, 111:110019, 2020.

[33] H. Mohammadi and F. Bahramian. Boundary conditions in simulation of stenosed coronary arteries. *Cardiovasc Eng*, 9(3):83–91, 2009. 1573-6806 Mohammadi, Hadi Bahramian, Fereshteh Journal Article Research Support, Non-U.S. Gov't Netherlands 2009/08/19 Cardiovasc Eng. 2009 Sep;9(3):83-91. doi: 10.1007/s10558-009-9078-z. Epub 2009 Aug 18.

[34] Iqbal Husain, Fotini Labropulu, Chris Langdon, and Justin Schwark. A comparison of newtonian and non-newtonian models for pulsatile blood flow simulations. *Journal of the Mechanical Behaviour of Materials*, 21:147–153, 2013.

[35] L. Antiga and D. A. Steinman. Rethinking turbulence in blood. *Biorheology*, 46(2):77–81, 2009. Antiga, Luca Steinman, David A Journal Article Research Support, Non-U.S. Gov't Netherlands Biorheology. 2009;46(2):77-81. doi: 10.3233/BIR-2009-0538.

[36] Raymond J Trudnowski and Rodolfo C Rico. Specific gravity of blood and plasma at 4 and 37 °c. *Clinical Chemistry*, 20(5):615–616, 1974.

[37] Alvin H. Sacks and E. Glenn Tickner. The compressibility of blood. *Biorheology*, 5:271–274, 1968.

[38] T. Kenner. The measurement of blood density and its meaning. *Basic Research in Cardiology*, 84(2):111–124, 1989.

[39] Chen Chong, Yan Xiong, Wentao Jiang, Yunbing Wang, Zhenze Wang, and yu Chen. Experimental and numerical simulation of biodegradable stents with different strut geometries. *Cardiovascular Engineering and Technology*, 11, 2019.

[40] N. S. Ribeiro, J. Folgado, and H. C. Rodrigues. Surrogate-based visualization and sensitivity analysis of coronary stent performance: A study on the influence of geometric design. *Int J Numer Method Biomed Eng*, 34(10):e3125, 2018. 2040-7947 Ribeiro, Nelson S Orcid: 0000-0002-2018-7007 Folgado, João Rodrigues, Hélder C Journal Article Research Support, Non-U.S. Gov't England Int J Numer Method Biomed Eng. 2018 Oct;34(10):e3125. doi: 10.1002/cnm.3125. Epub 2018 Jul 25.

[41] C. Lally, F. Dolan, and P. J. Prendergast. Cardiovascular stent design and vessel stresses: a finite element analysis. *J Biomech*, 38(8):1574–81, 2005. Lally, C Dolan, F Prendergast, P J Comparative Study Evaluation Study Journal Article Research Support, Non-U.S. Gov't United States J Biomech. 2005 Aug;38(8):1574-81. doi: 10.1016/j.jbiomech.2004.07.022.

[42] Jr. Coulter, N. A. and J. R. Pappenheimer. Development of turbulence in flowing blood. *Am J Physiol*, 159(2):401–8, 1949. COULTER, N A Jr Pappenheimer, j r Journal Article United States Am J Physiol. 1949 Nov;159(2):401-8. doi: 10.1152/ajplegacy.1949.159.2.401.

[43] R. Mongrain, I. Faik, R. L. Leask, J. Rodés-Cabau, E. Larose, and O. F. Bertrand. Effects of diffusion coefficients and struts apposition using numerical simulations for drug eluting coronary stents. *J Biomech Eng*, 129(5):733–42, 2007. Mongrain, Rosaire Faik, Isam Leask, Richard L Rodés-Cabau, Josep Larose, Eric Bertrand, Olivier F Journal Article Research Support, Non-U.S. Gov't United States J Biomech Eng. 2007 Oct;129(5):733-42. doi: 10.1115/1.2768381.

[44] Yunlong Huo and Ghassan S. Kassab. A hybrid one-dimensional/womersley model of pulsatile blood flow in the entire coronary arterial tree. *American Journal of Physiology-Heart and Circulatory Physiology*, 292(6):H2623–H2633, 2007. PMID: 17208998.

[45] Matt Sinnott, Paul Cleary, and Mahesh Prakash. *An investigation of pulsatile blood flow in a bifurcation artery using a grid-free method*. 2006.

[46] Chih-Hao Liu, Kuen-Hau Lin, Hao-Chueh Mai, and Chao-An Lin. Thermal boundary conditions for thermal lattice boltzmann simulations. *Computers Mathematics with Applications*, 59:2178–2193, 04 2010.